

Discrimination of dark matter models in future experiments

Tomohiro Abe¹, Ryuichiro Kitano^{1,2} and Ryosuke Sato¹

¹*Institute of Particle and Nuclear Studies,
High Energy Accelerator Research Organization (KEK)
Tsukuba 305-0801, Japan*

²*The Graduate University for Advanced Studies (Sokendai)
Tsukuba 305-0801, Japan*

Abstract

Phenomenological aspects of simple dark matter models are studied. We discuss ways to discriminate the dark matter models in future experiments. We find that the measurements of the branching fraction of the Higgs boson into two photons and the electric dipole moment of the electron as well as the direct detection experiments are quite useful in discriminating particle models of dark matter. We also discuss the prospects of finding new particles in dark sector at the LHC/ILC.

Contents

1	Introduction	3
2	Dark Matter Models	4
2.1	Singlet scalar dark matter (Model S1)	5
2.2	Doublet scalar dark matter (Model S2)	5
2.3	Triplet scalar / fermion model (Model S3, F3)	6
2.4	Singlet-doublet fermion dark matter (Model F12)	7
2.5	Doublet-triplet fermion dark matter (Model F23)	8
3	Phenomenology in each models	9
3.1	Model S1	10
3.1.1	Relic abundance and direct detection	11
3.1.2	Higgs invisible decay	11
3.2	Model S2	12
3.2.1	Relic abundance and direct detection	12
3.2.2	Direct search	13
3.2.3	S and T parameters	14
3.2.4	Higgs invisible decay	16
3.2.5	Higgs diphoton decay signal	17
3.3	Model F12	18
3.3.1	Relic abundance and direct detection	18
3.3.2	Higgs invisible decay	22
3.3.3	S and T parameters	24
3.3.4	Electric dipole moment	24
3.3.5	Direct search	27
3.4	Model F23	27
3.4.1	Relic abundance and direct detection	28
3.4.2	Higgs diphoton decay signal	28

4	Discrimination of model S1 and F12	29
4.1	$m_{\text{DM}} \lesssim 53 \text{ GeV}$	30
4.2	$53 \text{ GeV} \lesssim m_{\text{DM}} \lesssim m_h/2$	30
4.3	$100 \text{ GeV} \lesssim m_{\text{DM}}$	30
5	Conclusion and discussions	32
A	Loop functions	33
A.1	Loop functions for oblique corrections	34
A.2	Loop functions for diphoton signal	35

1 Introduction

Dark matter (DM) was first proposed by Oort [1] and Zwicky [2] to explain the motion of stars in our galaxy or galaxies in clusters. Eighty years have passed since then, and various evidences (e.g., galaxy rotation curves, gravitational lensing, precision measurement of cosmic microwave background and so on) support the existence of the dark matter. However, we still do not know what the dark matter is. Various candidates have been proposed. The most promising one is weakly interacting massive particle (WIMP) [3]. Since there is no candidate of such a particle in the standard model (SM), this scenario requires an extension of the SM.

The recent discovery of the Higgs boson and the measurements of its properties strongly support the origin of the Higgs boson as a component of the $SU(2)_L$ doublet Higgs field. Precise measurements of its properties to understand the nature of the Higgs field are one of the most important tasks in particle physics. It is quite possible that the DM particle couples to the SM through the Higgs field so that the DM abundance is explained as thermal relic *à la* the WIMP scenario. In that case, the Higgs boson as well as other SM particles carries information on the DM. In literature, such kind of various particle models have been proposed and their phenomenology have been studied, for example [4, 5, 6, 7, 9, 10, 11, 12, 13, 14, 15, 16, 17].

In this paper, we survey simple extensions of the SM to account for dark matter of the Universe by the WIMP scenario, and summarize the current situations and future

Table 1: List of dark matter models. Numbers in a parenthesis attached to the field represent $SU(2)_L \times U(1)_Y$ representation. For the Lagrangian of each model, see each section.

Model	Z_2 odd field(s)	Parameters
S1 (Sec. 2.1)	$s(1_0)$	m_s, λ_{sH}
S2 (Sec. 2.2)	$H_2(2_{1/2})$	$m_{A^0}, m_{S^0}, m_{H^+}, \lambda_A, \lambda_2$
F12 (Sec. 2.4)	$\psi_S(1_0), \psi_D(2_{-1/2}), \chi_D(2_{1/2})$	$m_S, m_D, \lambda, \lambda', \theta$
F23 (Sec. 2.5)	$\psi_D(2_{-1/2}), \chi_D(2_{1/2}), \psi_T(3_0)$	$m_D, m_T, \lambda, \lambda', \theta$

prospects to observe signatures of each model. We list six renormalizable models to realize the WIMP scenario as examples, and compare the model predictions to see if we can distinguish models by various measurements. We review and summarize the status of each model thoroughly, and also show new results such as the predictions to the electron electric dipole moment (EDM) in the fermionic dark matter models. We examine which observables are important in each models, and discuss the differences.

This paper is organized as follows. In section 2, we introduce dark matter models which we will discuss in this paper. In section 3, we briefly review phenomenology in each models, especially focusing on the spin-independent cross section, Higgs invisible decay, Higgs diphoton signal, and electron EDM. We impose in each model that the energy density of the dark matter abundances $\Omega_{\text{DM}} h^2 = 0.1196 \pm 0.0031$ which is reported by the Planck collaboration [18] is explained. In section 4, we discuss how to discriminate models in future experiments Section 5 is devoted for conclusion and discussions.

2 Dark Matter Models

In this section, we list dark matter models which we discuss in this paper. We add new field(s) to the SM and introduce Z_2 parity which guarantees the stability of the dark matter. Under this Z_2 parity, all of the SM fields are even and the new fields are odd. We take minimal renormalizable Lagrangian which includes a candidate of dark matter. We summarize the models in Tab. 1.

2.1 Singlet scalar dark matter (Model S1)

In this model, an additional $SU(2)_L$ singlet real scalar s with hypercharge $Y = 0$ is introduced [4, 5, 6]. Mass and interaction terms for s are given by,

$$\mathcal{L}_{S1} = -\frac{m_1^2}{2}s^2 - \frac{\lambda_{sH}}{2}s^2|H|^2 - \frac{\lambda_s}{4!}s^4. \quad (1)$$

The self-interaction term, s^4 , does not affect following discussion. The mass eigenvalue of s is given by $m_s^2 = m_1^2 + \lambda_{sH}v^2/2$, where $v \simeq 246$ GeV is the VEV of the Higgs field.

2.2 Doublet scalar dark matter (Model S2)

In this model, an additional $SU(2)_L$ doublet scalar H_2 with hypercharge $Y = 1/2$ is introduced [8, 9]. Mass and interaction terms for H_2 are given by,

$$\mathcal{L}_{S2} = -m_2^2|H_2|^2 - \lambda_1|H|^4 - \lambda_2|H_2|^4 - \lambda_3|H|^2|H_2|^2 - \lambda_4|H^\dagger H_2|^2 - \frac{\lambda_5}{2}[(H_2^\dagger H)^2 + h.c.]. \quad (2)$$

In general, λ_5 is a complex parameter, however, its phase can be taken away by a re-definition of H_2 . In the following of this paper, we take λ_5 as real and positive. H_2 is decomposed as,

$$H_2 = \begin{pmatrix} H^+ \\ (S^0 + iA^0)/\sqrt{2} \end{pmatrix}, \quad (3)$$

where H^+ is a charged scalar field and S^0 and A^0 are neutral real scalar fields. In the unitary gauge, the interaction terms between additional scalar particles and the Higgs boson are given by,

$$\begin{aligned} \mathcal{L}_{S2} \ni & -\lambda_3|H|^2|H_2|^2 - \lambda_4|H^\dagger H_2|^2 - \frac{\lambda_5}{2}[(H_2^\dagger H)^2 + h.c.] \\ & = -\lambda_3|H^+|^2 \left(\frac{v+h}{\sqrt{2}}\right)^2 - \frac{\lambda_S}{2}s^2 \left(\frac{v+h}{\sqrt{2}}\right)^2 - \frac{\lambda_A}{2}a^2 \left(\frac{v+h}{\sqrt{2}}\right)^2, \end{aligned} \quad (4)$$

where $\lambda_S \equiv \lambda_3 + \lambda_4 + \lambda_5$ and $\lambda_A \equiv \lambda_3 + \lambda_4 - \lambda_5$ are effective couplings to the Higgs boson. Mass eigenvalues of them are given by,

$$m_{H^+}^2 = m_2^2 + \frac{\lambda_3}{2}v^2, \quad m_{S^0}^2 = m_2^2 + \frac{\lambda_S}{2}v^2, \quad m_{A^0}^2 = m_2^2 + \frac{\lambda_A}{2}v^2. \quad (5)$$

$\lambda_A < \lambda_S$ and $m_{A^0} < m_{S^0}$ are satisfied because we take λ_5 as real and positive. Furthermore, if $\lambda_4 < \lambda_5$, A^0 becomes lighter than H^+ . In this situation, A^0 becomes the candidate of dark matter. Conditions for the scalar potential to be bounded from below are given by [9],

$$\min[\lambda_A, \lambda_S, \lambda_3] = \lambda_A > -2\sqrt{\lambda_1\lambda_2}, \quad \lambda_2 > 0.$$

2.3 Triplet scalar / fermion model (Model S3, F3)

If we add $SU(2)$ triplet scalar (t) / fermion (χ) with $Y = 0$, we can construct simple dark matter models¹ [13, 19]. Here, we call them as model S3 and F3, respectively. Model F3 is an effective theory of wino dark matter model [20, 21]. Lagrangian of each models are given by,

$$\mathcal{L}_{S3} = \mathcal{L}_{SM} + \frac{1}{2}(\partial t)^2 - \frac{m_3^2}{2}t^2 - \frac{\lambda_{tH}}{2}t^2|H|^2, \quad (6)$$

$$\mathcal{L}_{F3} = \mathcal{L}_{SM} + i\psi_T\bar{\psi}_T - \left(\frac{M_T}{2}\psi_T\psi_T + h.c.\right). \quad (7)$$

In model S3, we can write the dark matter self interaction term t^4 . However, this self-interaction term does not affect our discussion, and thus we neglect it.

Model S3 has a neutral scalar t^0 and a charged scalar t^+ , and model F3 has a neutral Majorana fermion ψ_T^0 and a charged Dirac fermion ψ_T^+ . In both of the models, masses of the neutral particle and the charged particle are degenerated. Mass splitting between them is generated by one-loop radiative correction [19]. In model S3, for $m_{t^0}, m_{t^\pm} \gg m_W, m_Z$,

$$m_{t^+} - m_{t^0} \simeq \frac{\alpha_2}{2} (m_W - c_W^2 m_Z) \simeq 166 \text{ MeV}, \quad (8)$$

and, in model F3, for $m_{\chi^0}, m_{\chi^\pm} \gg m_W, m_Z$,

$$m_{\psi_T^+} - m_{\psi_T^0} \simeq \frac{\alpha_2}{2} (m_W - c_W^2 m_Z) \simeq 166 \text{ MeV}. \quad (9)$$

Hence, in both of the models, charged particles becomes slightly heavier than neutral ones. In such a situation, dark matter coannihilation becomes important to obtain a

¹One might think model F2, namely $SU(2)$ doublet Dirac fermion with $Y = 1/2$ is also simple possibility. However, a dark matter with non-zero hypercharge is severely constrained by the direct detection experiments [19].

correct amount of thermal relic abundance, and thus the mass of the dark matter tends to be large. We can get correct relic abundance for $m_{t^0} \sim 2.5$ TeV in model S3, and $m_{\psi_T^0} \sim 2.7$ TeV in model F3 [14]. It is difficult to discuss them in near future collider experiment. Hence, we do not discuss them in detail.

2.4 Singlet-doublet fermion dark matter (Model F12)

Here, we discuss singlet-doublet mixed fermion dark matter model [15, 16]. We introduce three left-handed Weyl fermions; SM singlet fermion (ψ_S), $SU(2)_L$ doublet fermion with $Y = -1/2$ (ψ_D) and $Y = 1/2$ (χ_D). This matter content is vector-like, and this model is free from gauge anomaly. Renormalizable interaction terms of dark matter sector are given by,

$$\mathcal{L}_{\text{F12}} = -\frac{1}{2}m_S\psi_S\psi_S - m_D\psi_D\chi_D + y\tilde{H}^\dagger\psi_S\psi_D + y'H^\dagger\psi_S\chi_D + h.c., \quad (10)$$

where $\tilde{H} = \epsilon H^*$ and ϵ is totally antisymmetric tensor. We have four complex parameters in the dark matter sector. Among them, three phases can be removed by a redefinition of ψ_S , ψ_D and χ_D . In this paper, we take a basis in which m_S , m_D and y are real positive. Finally, we have the following five physical free parameters in this model,

$$m_S, m_D, y, |y'|, \theta \equiv \arg(y'). \quad (11)$$

In this model, we have one charged Dirac fermion and three Majorana neutral fermions. Mass of the charged fermion is m_D . Mass eigenstates of the neutral fermions are the mixture of ψ_S , ψ_D^0 and χ_D^0 . Mass matrix of them is given by,

$$\mathcal{L}_{\text{mass}} = -\frac{1}{2} \begin{pmatrix} \psi_S & \psi_D^0 & \chi_D^0 \end{pmatrix} \begin{pmatrix} m_S & yv/\sqrt{2} & -y'v/\sqrt{2} \\ yv/\sqrt{2} & 0 & -m_D \\ -y'v/\sqrt{2} & -m_D & 0 \end{pmatrix} \begin{pmatrix} \psi_S \\ \psi_D^0 \\ \chi_D^0 \end{pmatrix}. \quad (12)$$

Mass eigenstates f 's can be written as linear combination of ψ_S , ψ_D^0 and χ_D^0 :

$$\begin{pmatrix} \psi_S \\ \psi_D^0 \\ \chi_D^0 \end{pmatrix} = \begin{pmatrix} U_{11} & U_{12} & U_{13} \\ U_{21} & U_{22} & U_{23} \\ U_{31} & U_{32} & U_{33} \end{pmatrix} \begin{pmatrix} f_1^0 \\ f_2^0 \\ f_3^0 \end{pmatrix}, \quad (13)$$

where U is a unitary matrix. We define the following four-component Dirac and Majorana spinors:

$$\Psi^+ \equiv \begin{pmatrix} \chi_D^+ \\ \psi_D^{-\dagger} \end{pmatrix}, \quad \Psi_i^0 \equiv \begin{pmatrix} f_i^0 \\ f_i^{0\dagger} \end{pmatrix}, \quad (14)$$

Relevant interaction terms for the calculation of S , T parameters and EDM are given by,

$$\begin{aligned} \mathcal{L}_{\text{int.}} = & g \bar{\Psi}^+ \gamma^\mu (\mathcal{C}_{L,i} P_L + \mathcal{C}_{R,i} P_R) \Psi_i^0 W_\mu^+ + g \bar{\Psi}_i^0 \gamma^\mu (\mathcal{C}_{L,i}^* P_L + \mathcal{C}_{R,i}^* P_R) \Psi^+ W_\mu^- \\ & + \frac{g}{2c_W} \bar{\Psi}_i^0 \gamma^\mu (\mathcal{N}_{L,ij} P_L + \mathcal{N}_{R,ij} P_R) \Psi_j^0 Z_\mu + \frac{g}{c_W} \left(\frac{1}{2} - s_W^2 \right) \bar{\Psi}^+ \gamma^\mu \Psi^+ Z_\mu, \end{aligned} \quad (15)$$

where $\mathcal{C}_{L,i}$, $\mathcal{C}_{R,i}$, $\mathcal{N}_{L,ij}$ and $\mathcal{N}_{R,ij}$ are determined by the mixing matrix U :

$$\mathcal{C}_{L,i} = \frac{1}{\sqrt{2}} U_{3i}, \quad \mathcal{C}_{R,i} = -\frac{1}{\sqrt{2}} U_{2i}^*, \quad \mathcal{N}_{L,ij} = -\mathcal{N}_{R,ji} = \frac{1}{2} (U_{3i}^* U_{3j} - U_{2i}^* U_{2j}). \quad (16)$$

Let us comment on symmetry in this model. In the case of $\theta = 0$ or π , we can take all of the parameters in the dark matter sector as real by using redefinition of ψ_S , ψ_D and χ_D , *i.e.*, CP is conserved in dark matter sector. On the other hand, in the cases of $\theta \neq 0, \pi$, the dark matter sector does violate CP symmetry. The dark matter sector gives contribution to EDMs of the SM particles. If $y = |y'|$, we have charge conjugation symmetry as $\psi_D \leftrightarrow \chi_D$. In this case, dark matter-dark matter- Z boson coupling vanishes. Furthermore, ψ_D and χ_D form an $SU(2)_R$ doublet and dark matter sector has custodial symmetry in this case, and the contribution of Z_2 odd particles to T -parameter vanishes at the one-loop level.

2.5 Doublet-triplet fermion dark matter (Model F23)

Here, we discuss doublet-triplet mixed fermion dark matter model [17]. We introduce three left-handed Weyl fermions; $SU(2)_L$ doublet fermion with $Y = -1/2$ (ψ_D) and $Y = 1/2$ (χ_D) and $SU(2)_L$ triplet fermion (ψ_T) with $Y = 0$. This matter content is vector-like, and thus, it is free from gauge anomaly. Renormalizable interaction terms in the dark matter sector are given by,

$$\mathcal{L}_{\text{F23}} = -\frac{1}{2} m_S \psi_T \psi_T - m_D \psi_D \chi_D + y \tilde{H}^\dagger \psi_T \psi_D + y' H^\dagger \psi_T \chi_D + h.c. \quad (17)$$

We have four complex parameters in the dark matter sector. Among them, three phases can be removed by a redefinition of ψ_D , χ_D and ψ_T . In this paper, we take a basis in which

m_D , m_T and y are real and positive. In this basis, we have the following five physical free parameters,

$$m_D, m_T, y, |y'|, \theta \equiv \arg(y'). \quad (18)$$

In this model, there are two charged Dirac fermions and three Majorana neutral fermions. Mass matrices of the fermions are given by,

$$\begin{aligned} \mathcal{L}_{\text{mass}} = & -\frac{1}{2} \begin{pmatrix} \psi_D^0 & \chi_D^0 & \psi_T^0 \end{pmatrix} \begin{pmatrix} 0 & -m_D & yv/\sqrt{2} \\ -m_D & 0 & -y'v/\sqrt{2} \\ yv/\sqrt{2} & -y'v/\sqrt{2} & m_T \end{pmatrix} \begin{pmatrix} \psi_D^0 \\ \chi_D^0 \\ \psi_T^0 \end{pmatrix} \\ & - \begin{pmatrix} \chi_D^+ & \psi_T^+ \end{pmatrix} \begin{pmatrix} m_D & y'v \\ yv & m_T \end{pmatrix} \begin{pmatrix} \psi_D^- \\ \psi_T^- \end{pmatrix}. \end{aligned} \quad (19)$$

Mass eigenstates f 's can be written as linear combinations of ψ_D , χ_D and ψ_T :

$$\begin{pmatrix} \psi_D^0 \\ \chi_D^0 \\ \psi_T^0 \end{pmatrix} = \begin{pmatrix} U_{11}^0 & U_{12}^0 & U_{13}^0 \\ U_{21}^0 & U_{22}^0 & U_{23}^0 \\ U_{31}^0 & U_{32}^0 & U_{33}^0 \end{pmatrix} \begin{pmatrix} f_1^0 \\ f_2^0 \\ f_3^0 \end{pmatrix}, \quad (20)$$

$$\begin{pmatrix} \chi_D^+ \\ \psi_T^+ \end{pmatrix} = \begin{pmatrix} U_{11}^+ & U_{12}^+ \\ U_{21}^+ & U_{22}^+ \end{pmatrix} \begin{pmatrix} f_1^+ \\ f_2^+ \end{pmatrix}, \quad \begin{pmatrix} \psi_D^- \\ \psi_T^- \end{pmatrix} = \begin{pmatrix} U_{11}^- & U_{12}^- \\ U_{21}^- & U_{22}^- \end{pmatrix} \begin{pmatrix} f_1^- \\ f_2^- \end{pmatrix}, \quad (21)$$

where U^0 , U^+ and U^- are unitary matrices. We define the following four-component Dirac and Majorana spinors:

$$\Psi_i^+ \equiv \begin{pmatrix} f_i^+ \\ f_i^{-\dagger} \end{pmatrix}, \quad \Psi_i^0 \equiv \begin{pmatrix} f_i^0 \\ f_i^{0\dagger} \end{pmatrix}. \quad (22)$$

The situation is similar to the model F12 regarding of phases and custodial symmetry. In the case of $\theta = 0$ and π , we can take all the parameters in the dark matter sector as real by using redefinitions of ψ_D , χ_D and ψ_T . For $y = |y'|$, we have charge conjugation symmetry as $\psi_D \leftrightarrow \chi_D$, which results in vanishing dark matter-dark matter- Z boson coupling. Due to the custodial symmetry at that point, the contribution of Z_2 odd particles to the T -parameter vanishes at the one-loop level.

3 Phenomenology in each models

In this section, we discuss phenomenological aspects of the dark matter models which are introduced in the previous section. In the following analysis, we used FeynRules [22]

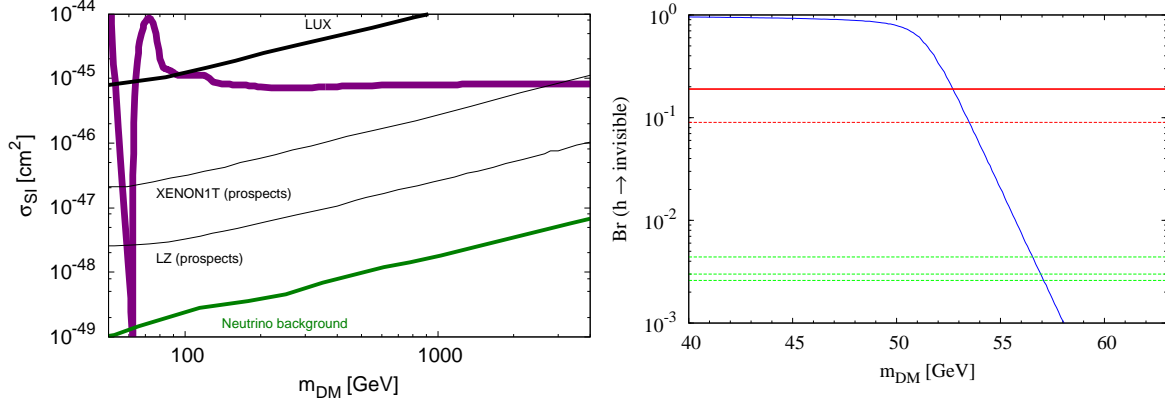


Figure 1: Present status of scalar dark matter S1 model. **Left:** The wide mass range of the dark matter mass is shown. The purple line is the model prediction. The black bold solid line is current bound by the LUX experiment. The green line shows the discovery limit which is caused by atmospheric and astrophysical neutrinos. We also plot future prospect of XENON1T and LZ. **Right:** The branching fraction of the Higgs invisible decay in S1 model. The red solid line is the current bound. The red dashed line is the future prospect of LHC at 300 fb^{-1} . The three green dashed lines are the future prospect of the ILC. (250 GeV with 250 fb^{-1} , 500 GeV with 500 fb^{-1} , 1 TeV with 1 ab^{-1} .)

and micrOMEGAs [23] for the calculation of relic abundance of dark matter and Higgs invisible decay width. We take the Higgs boson mass as 125 GeV [24, 25] throughout this paper.

3.1 Model S1

In the model S1, there are only two parameters which are relevant to dark matter physics, *i.e.*, the dark matter mass m_{DM} and the dark matter-Higgs coupling λ_{sH} . By imposing the condition that the relic abundance explains the DM of the Universe, λ_{sH} is fixed as a function of m_{DM} , and thus m_{DM} is the only free parameter. In the following we compute the direct detection cross section as a function of the dark matter mass. If the dark matter mass is smaller than a half of the Higgs boson mass, the Higgs boson can decay into two dark matter particles. This contributes to the branching fraction of the invisible decay of the Higgs boson. We also discuss it here.

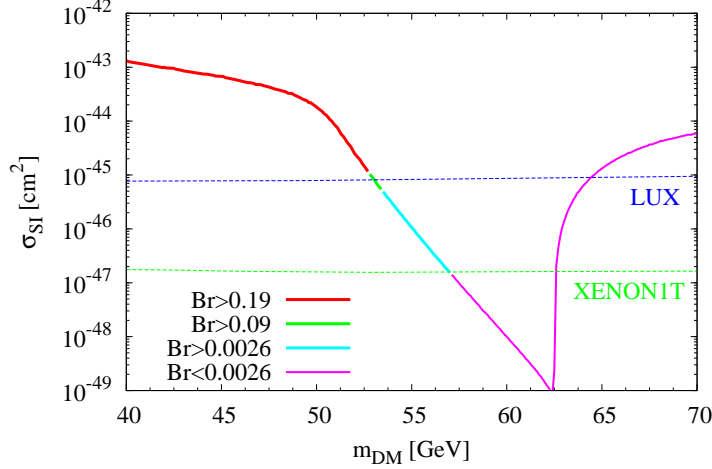


Figure 2: The dark matter mass around a half of the Higgs mass is shown. The line shows the parameter regions which can realize $\Omega_{\text{DM}} h^2 = 0.12029$ [18]. The red, green, cyan, and purple solid lines are $0.19 < \text{Br}(h \rightarrow \text{invisible})$, $0.09 < \text{Br}(h \rightarrow \text{invisible}) < 0.19$, $0.0026 < \text{Br}(h \rightarrow \text{invisible}) < 0.09$, and $\text{Br}(h \rightarrow \text{invisible}) < 0.0026$, respectively. The green and blue dashed lines are the current bound by the LUX experiment and future prospect of XENON 1T.

3.1.1 Relic abundance and direct detection

Here, we show the constraint on the spin independent cross section (σ_{SI}) from the LUX experiment [26]. The left panel of Fig. 1 shows σ_{SI} as a function of the dark matter mass m_{DM} where the correct dark matter abundance is imposed. The mass region with $53 \text{ GeV} \lesssim m_{\text{DM}} \lesssim 64 \text{ GeV}$ and $100 \text{ GeV} \lesssim m_{\text{DM}}$ are allowed by the constraint from the LUX experiment. We also show the future prospects of XENON1T and LZ [27], and the dark matter discovery limit which is caused by atmospheric and astrophysical neutrinos [28].

3.1.2 Higgs invisible decay

The right panel in Fig. 1 shows the branching fraction of the Higgs invisible decay as a function of the dark matter mass m_{DM} while the requiring the correct dark matter abundance. The current bound on the branching fraction of the invisible decay of the Higgs boson in model S1 is $\text{Br}(h \rightarrow \text{invisible}) < 0.19$ [12]. This is shown with the red solid line in the figure. Thus the lower bound on the dark matter mass is 53 GeV that coincides

the one from the LUX experiment. The LHC can reach $\text{Br} = 0.09$ with 300 fb^{-1} [29], and the ILC can reach $\text{Br}=0.0026$ with $\sqrt{s} = 1 \text{ TeV}$ and 1 ab^{-1} [29]. These lines are shown in the figure.

In the Fig. 2, we focus on the light DM mass region. The information on the branching fraction of the Higgs invisible decay is also shown. We see that XENON1T will cover the ILC reach. Therefore, in this model, if XENON1T finds the DM signal in this region, the ILC should also find the Higgs invisible decay.

3.2 Model S2

In model S2, the dark matter couplings to the SM particles are determined by $SU(2)_L \times U(1)_Y$ gauge couplings and λ_A which is defined in Sec. 2.2. After fixing the size of λ_A by the relic abundance, we discuss the spin independent cross section at the direct detection experiments. We find that there are two dark matter mass regions, $m_{\text{DM}} \lesssim 72 \text{ GeV}$ and $m_{\text{DM}} \gtrsim 600 \text{ GeV}$. We also discuss the mass bound on m_{H^+} and m_{S^0} from LEP2 and electroweak precision bounds. Then we focus on the light dark matter mass region and discuss the contribution of the dark matter to the branching fraction of the invisible decay, and the diphoton channel of the Higgs boson. We will find the branching fraction of the invisible decay has similar behavior as the S1 model, and the signal strength of $h \rightarrow \gamma\gamma$ is $\sim 10\%$ smaller than the one in the SM.

3.2.1 Relic abundance and direct detection

We have four free parameters, $m_{\text{DM}}(= m_{A^0})$, m_{S^0} , m_{H^+} and λ_A . The value of λ_A can be fixed by requiring the correct amount of relic abundance. We have three mass parameters left. In Fig. 3, we show the spin independent cross section σ_{SI} as a function of dark matter mass m_{DM} in the dark matter S2 model while requiring the correct dark matter abundance.

The parameter space which gives the correct amount of the dark matter is splitted into two regions; the light mass region $m_{\text{DM}} \lesssim 72 \text{ GeV}$ and the heavy mass region $m_{\text{DM}} \gtrsim 500 \text{ GeV}$. In the light mass region, the Higgs boson s -channel exchange diagrams give dominant contribution to the dark matter annihilation cross section. If $m_{S^0} - m_{A^0}$ and $m_{H^+} - m_{A^0}$ are large enough, as we can see from Fig. 3, the S2 dark matter has very similar

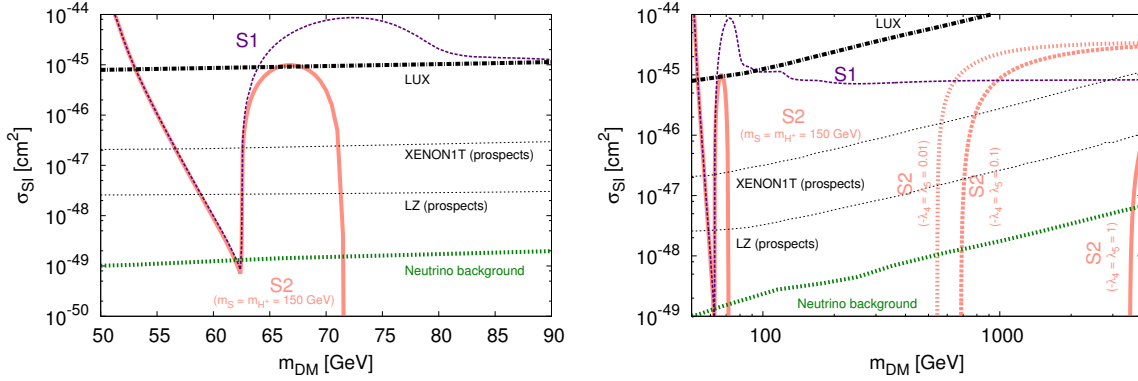


Figure 3: Present status of model S2. Each line shows the parameter regions which can realize $\Omega_{\text{DM}} h^2 = 0.12029$ [18]. Purple dotted line shows model S1, pink lines shows model S2. In left figure, we take $m_{S^0} = m_{H^\pm} = 150$ GeV. In right figure, we take $m_{S^0} = m_{H^\pm} = 150$ GeV for leftmost pink line. For other lines, we take $-\lambda_4 = \lambda_5$ as 0.01, 0.1 and 1 from left to right. Black chain line shows the constraint from the LUX. Green dotted lines show the discovery limit which is caused by atmospheric and astrophysical neutrinos [28]. We also plot future prospect of XENON1T and LZ [27].

behaviour to S1 dark matter at the tree level calculation. However, for $m_{\text{DM}} \sim m_h/2$ (*i.e.*, small λ_A), it is pointed out that one-loop radiative corrections give significant modification on the spin independent cross section for model S2 dark matter [30], because it is charged under the electroweak gauge group. In the figure, the tree level cross section is shown. For $m_{\text{DM}} > m_W$, $A^0 A^0 \rightarrow W^+ W^-$ channel opens and the annihilation cross section becomes large. Therefore unlike the model S1, the abundance of S2 dark matter becomes too small to explain $\Omega_{\text{DM}} h^2$ for $m_{\text{DM}} \gtrsim m_W$. For $m_{\text{DM}} \gtrsim 500$ GeV, a viable region reappears. The relic abundance in the heavy mass region is very sensitive to mass splittings between dark matter and heavier particles S^0 and H^\pm .

3.2.2 Direct search

Now we determined two parameters, m_{DM} and λ_A by imposing the correct relic density. The remaining parameters are m_{H^\pm} and m_{S^0} .

At e^+e^- colliders, H^\pm can be produced by a process $e^+e^- \rightarrow (Z/\gamma)^* \rightarrow H^+H^-$. The LEP2 experiment gives the lower bound of the mass of H^\pm to be 70–90 GeV [31]. Also, neutral scalar bosons can be produced by a process $e^+e^- \rightarrow Z^* \rightarrow A^0 S^0$ [32]. See Fig. 4.

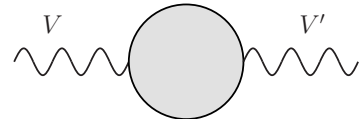
For the dark matter lighter than the W boson, we find that a viable parameter regions opens for $m_{S^0} - m_{A^0} \gtrsim 40$ GeV, and a small window around $m_{S^0} - m_{A^0} \simeq 8$ GeV.

For $65 \text{ GeV} < m_{\text{DM}} < 70 \text{ GeV}$, we see that the exclusion by the spin-independent cross section is sensitive to the charged Higgs mass. In this region, we need to take into account $A^0 A^0 \rightarrow WW^*$ process in the relic density. The diagram exchanging the charged Higgs in t -channel contributes to this process, and it is destructive with the same process with the Higgs boson in the s -channel. Therefore, the heavier charged Higgs requires the smaller Higgs coupling to the DM to reproduce the correct relic abundance, and thus the spin-independent cross section is also smaller when the charged Higgs is heavier and heavier. Note that the spin-independent cross section in this region is on the edge of the exclusion limit as we can see from Fig. 3.

At the LHC, the model S2 can be probed by searching for dilepton and missing energy signal [33] and trilepton and missing energy signal [34]. For $40 \text{ GeV} \lesssim m_{\text{DM}} \lesssim 72 \text{ GeV}$, this search has a sensitivity in the parameter region with $m_{H^+, S^0} \simeq 100\text{--}180 \text{ GeV}$.

3.2.3 S and T parameters

In this section, we discuss electroweak precision measurement. The gauge boson two-point functions are given as,



$$\text{wavy line } V \text{ --- } \text{grey circle} \text{ --- } \text{wavy line } V' = i\Pi_{VV'}(p^2)g^{\mu\nu} + i\Delta_{VV'}p^\mu p^\nu. \quad (23)$$

By using this, the Peskin-Takeuchi parameters [35] are defined as,

$$S = \frac{4s^2 c^2}{\alpha} \left(\frac{\Pi_{ZZ}(m_Z^2) - \Pi_{ZZ}(0)}{m_Z^2} - \frac{c^2 - s^2}{sc} \frac{\Pi_{Z\gamma}(m_Z^2)}{m_Z^2} - \frac{\Pi_{\gamma\gamma}(m_Z^2)}{m_Z^2} \right), \quad (24)$$

$$T = \frac{1}{\alpha} \left(\frac{\Pi_{WW}(0)}{m_W^2} - \frac{\Pi_{ZZ}(0)}{m_Z^2} \right). \quad (25)$$

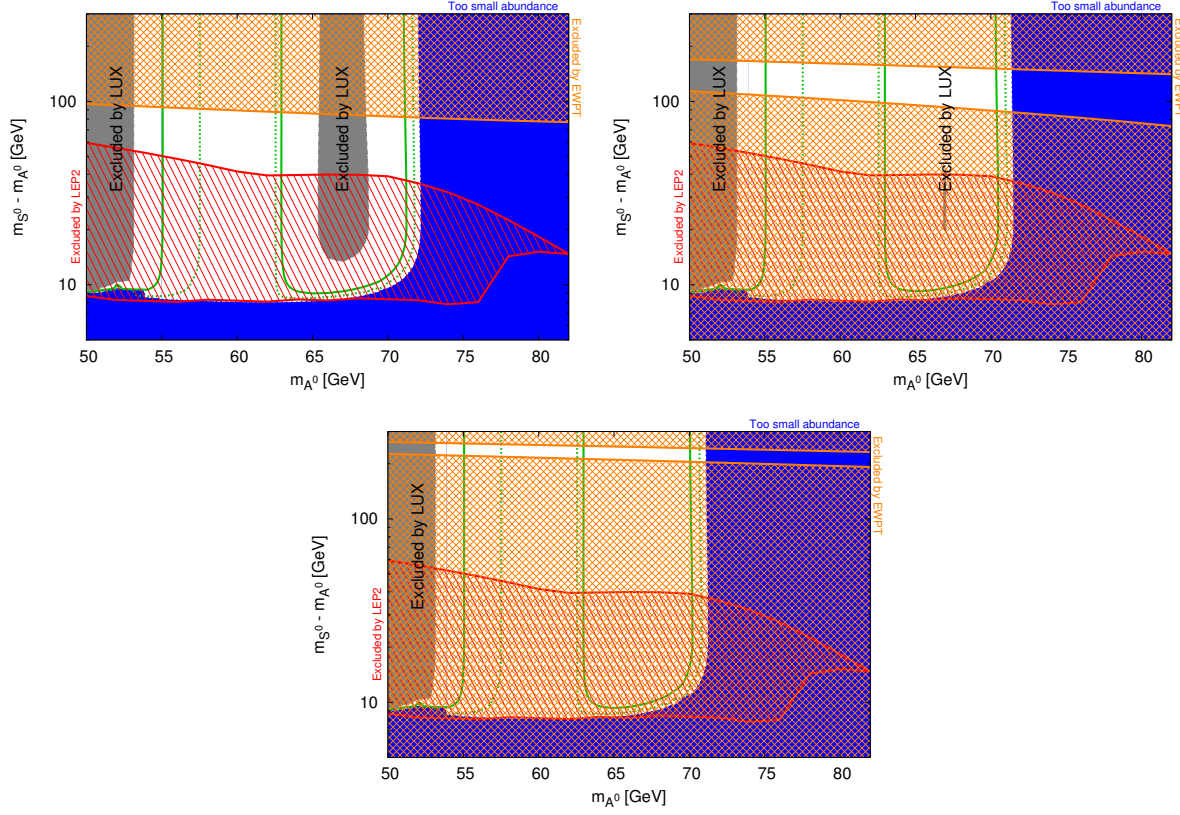


Figure 4: LEP2 constraint in $m_{A^0}-(m_{S^0}-m_{A^0})$ plane. In the blue regions, thermal relic abundance becomes too small. In this figure, we take $m_{H^+} = 120$ GeV (upper-left), $m_{H^+} = 200$ GeV (upper-right), and $m_{H^+} = 300$ GeV (lower). The red meshed regions are excluded by LEP2 experiment [32]. The gray regions are excluded by the LUX experiment. The yellow regions are excluded by S and T parameters. The green solid and the dotted lines show $\sigma_{\text{SI}} = 10^{-46}$ and 10^{-47} cm^2 , respectively.

The contributions to $\Pi_{VV'}$'s from the dark matter sector are given by,

$$\Pi_{WW} = \frac{g^2}{16\pi^2} \tilde{B}_{22}(m_{H^+}, m_s) + \frac{g^2}{16\pi^2} \tilde{B}_{22}(m_{H^+}, m_a), \quad (26)$$

$$\Pi_{ZZ} = \frac{1}{16\pi^2} \frac{g^2}{c^2} \left(\tilde{B}_{22}(m_s, m_a) + (c^2 - s^2)^2 \tilde{B}_{22}(m_{H^+}, m_{H^+}) \right), \quad (27)$$

$$\Pi_{Z\gamma} = \frac{eg}{c} \frac{c^2 - s^2}{8\pi^2} \tilde{B}_{22}(m_{H^+}, m_{H^+}), \quad (28)$$

$$\Pi_{\gamma\gamma} = \frac{e^2}{4\pi^2} \tilde{B}_{22}(m_{H^+}, m_{H^+}). \quad (29)$$

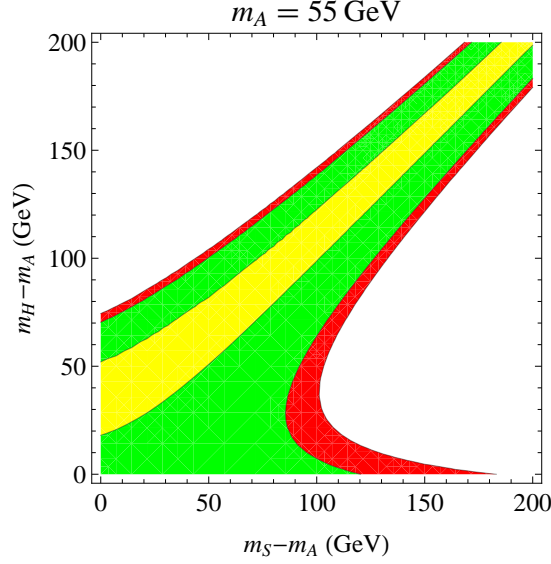


Figure 5: The constraint from the S and T parameters for $m_{\text{DM}} = 55$ GeV. The yellow, green, and red regions are allowed at 31.7% C.L., 90% C.L., and 95% C.L., respectively.

The definitions of \tilde{B}_{22} are given in the Appendix A.1². We show the numerical result of the constraint for $m_{\text{DM}} = 55$ GeV in Fig. 5. We find that large mass difference between the dark matter and other Z_2 odd particles are disfavored except for $m_{S^0} \sim m_{H^+}$ case. Note that when $m_{H^+} = m_{S^0}$, the custodial symmetry appears in the Z_2 odd sector, and thus the T parameter becomes zero at the one-loop level. The constraints are superimposed in Fig. 4.

3.2.4 Higgs invisible decay

Since there are viable parameter regions for $m_{A^0} < m_h/2$, we have a chance to observe the invisible decay of the Higgs boson. From the discussion on the LEP2 bound in Sec. 3.2.2 and the discussion on the electroweak precision bound in Sec. 3.2.3, it is natural to expect that $m_{S^0} \simeq m_{H^+} \gtrsim m_{\text{DM}} + 40$ GeV. Then the S2 dark matter has very similar behaviour to the S1 dark matter as we can see from Fig. 3. We conclude that the branching fraction of the Higgs invisible decay as a function of the dark matter mass in this model behaves same as in the S1 model shown in the right panel in Fig. 1.

²We have checked that our formulae are consistent with Ref. [9] in the limit of $m_{S^0}, m_{A^0}, m_{H^+} \gg m_Z$.

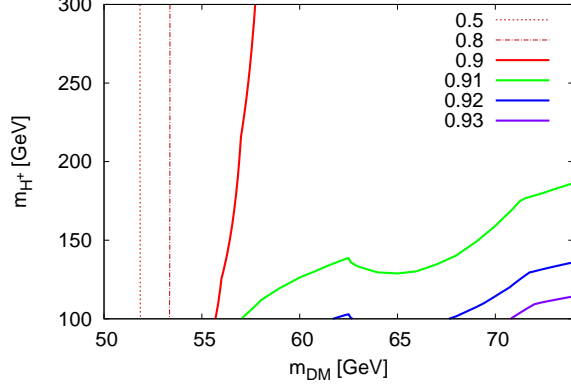


Figure 6: Diphoton signal strength $\mu \equiv \text{Br}(h \rightarrow 2\gamma)/\text{Br}(h \rightarrow 2\gamma; \text{SM})$ in $m_{\text{DM}}-m_{H^+}$ plane. In this figure, we take $m_{S^0} = m_{\text{DM}} + 100$ GeV.

3.2.5 Higgs diphoton decay signal

In model S2, loop diagrams including a charged scalar H^+ modify the branching fraction of the Higgs boson into two photons. Its decay width is given by [36, 37],

$$\Gamma(h \rightarrow 2\gamma) = \frac{G_F \alpha^2 m_h^3}{128 \sqrt{2} \pi^3} \left| A_{\text{SM}} + \frac{\lambda_3 v^2}{2m_{H^+}^2} A_0 \left(\frac{m_h^2}{4m_{H^+}^2} \right) \right|^2, \quad (30)$$

where the second term in the absolute value is the contribution from H^+ , and A_{SM} is the contribution from the SM particles, which is given by,

$$A_{\text{SM}} = A_1 \left(\frac{m_h^2}{4m_W^2} \right) + \sum_f N_C Q_f^2 A_{1/2}^H \left(\frac{m_h^2}{4m_f^2} \right), \quad (31)$$

and its numerical value is $A_{\text{SM}} \simeq -6.45$ for $m_h = 125$ GeV, $m_W = 80.4$ GeV and $m_t = 173$ GeV. The definition of the function A 's are given in the Appendix A.2. We can expect that the charged Higgs contribution does not decouple even if the charged Higgs mass is much larger than the electroweak scale as long as the mass difference between the dark matter and the charged Higgs mass is kept large. Because the mass differences among the Z_2 odd particles imply the sizable value of couplings of the Z_2 odd particles to the Higgs boson, namely sizable $\lambda_{3,4,5}$, the charged Higgs coupling to the Higgs boson remains even if its mass is quite large. We can confirm this expectation from Eq. (30).

By using Eq. (5), λ_3 can be written by m_{H^+} , m_{A^0} and λ_A ,

$$\frac{\lambda_3 v^2}{2m_{H^+}^2} = 1 - \frac{m_{A^0}^2}{m_{H^+}^2} + \frac{\lambda_A v^2}{2m_{H^+}^2}. \quad (32)$$

For $x \ll 1$, $A_0(x) \simeq 1/3 + 8x/45 + \dots$. Thus, as long as we consider light dark matter A^0 , even if the charged scalar is relatively heavy, the charged Higgs contribution remains and its asymptotic behavior is $\lambda_3 v^2 / (2m_{H^+}^2) A_0 \rightarrow 1/3$ ($m_{H^+} \rightarrow \infty$).

We show how the diphoton branching fraction is modified in Fig. 6. We find that the branching fraction to the diphoton channel deviates from the standard model around 10 %. Sensitivity to the diphoton signal strength is around 10 % at the LHC 14 TeV 300 fb⁻¹, and it reaches around 5 % at the ILC [38]. We can conclude that model S2 can be probed at the ILC in the case of $m_{\text{DM}} \lesssim 72$ GeV.

3.3 Model F12

In this section, we discuss phenomenological aspects of model F12. One of the features of this model is a CP-violating phase, and as we will see, it has important effects on dark matter phenomenology.

3.3.1 Relic abundance and direct detection

We show spin-independent direct detection cross section for model F12 in Fig. 7. Here we consider the case that the model gives the correct dark matter abundance. Similar to model S1 and S2, direct detection gives severe constraint on F12. In the case of the dark matter mass around $m_h/2$ and $m_Z/2$, the spin independent cross section becomes small. This is because, in these dark matter mass regions, diagrams with Higgs boson and Z boson in s -channel give the dominant contribution to the annihilation cross section, which requires small Higgs/ Z boson coupling to the DM.

In addition to this structure, the direct detection cross section shows complicated structures when we turn on the phase of the Yukawa coupling, θ . See, for example, 30 GeV $\lesssim m_{\text{DM}} \lesssim 50$ GeV region in the right panels in Fig. 7. We can understand this behavior as follows. The mass term and the interaction terms of the dark matter with

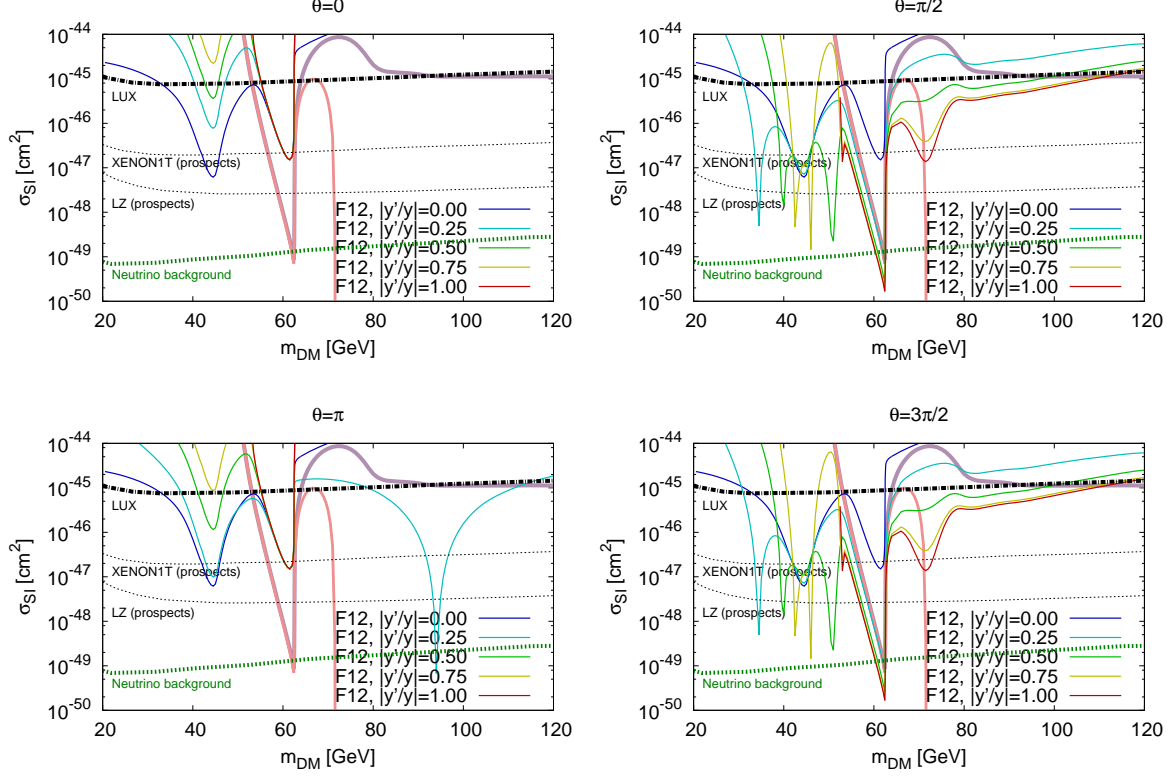


Figure 7: The spin independent cross section σ_{SI} of model F12. Blue, cyan, green, yellow, and red lines show $|y'/y| = 0, 0.25, 0.5, 0.75$ and 1 respectively. We take $m_D = 200$ GeV in these figures. For model F12, we take $\theta = 0$ (upper left), $\pi/2$ (upper right), π (lower left) and $3\pi/2$ (lower right). We also show σ_{SI} for model S1 (gray line) and model S2 with $m_{S^0} = m_{H^+} = m_{A^0} + 100$ GeV for references.

the SM particles are written as,

$$\mathcal{L} \ni -\frac{m_{\text{DM}}}{2} \bar{\Psi}_1^0 \Psi_1^0 + y_S h \bar{\Psi}_1^0 \Psi_1^0 + i y_P h \bar{\Psi}_1^0 \gamma^5 \Psi_1^0 + i c_Z Z_\mu \bar{\Psi}_1^0 \gamma^\mu \gamma^5 \Psi_1^0. \quad (33)$$

Here, y_S , y_P , and c_Z are calculated from λ , λ' and the unitary matrix U which is defined in Eq. (13). Although all couplings (y_S , y_P , and c_Z) contribute to the annihilation cross section, only y_S contributes to the spin independent cross section. This means that the spin independent cross section becomes zero while the correct relic abundance can be explained when $y_S = 0$, $y_P \neq 0$, and $c_Z \neq 0$. We found $y_S = 0$ when the following

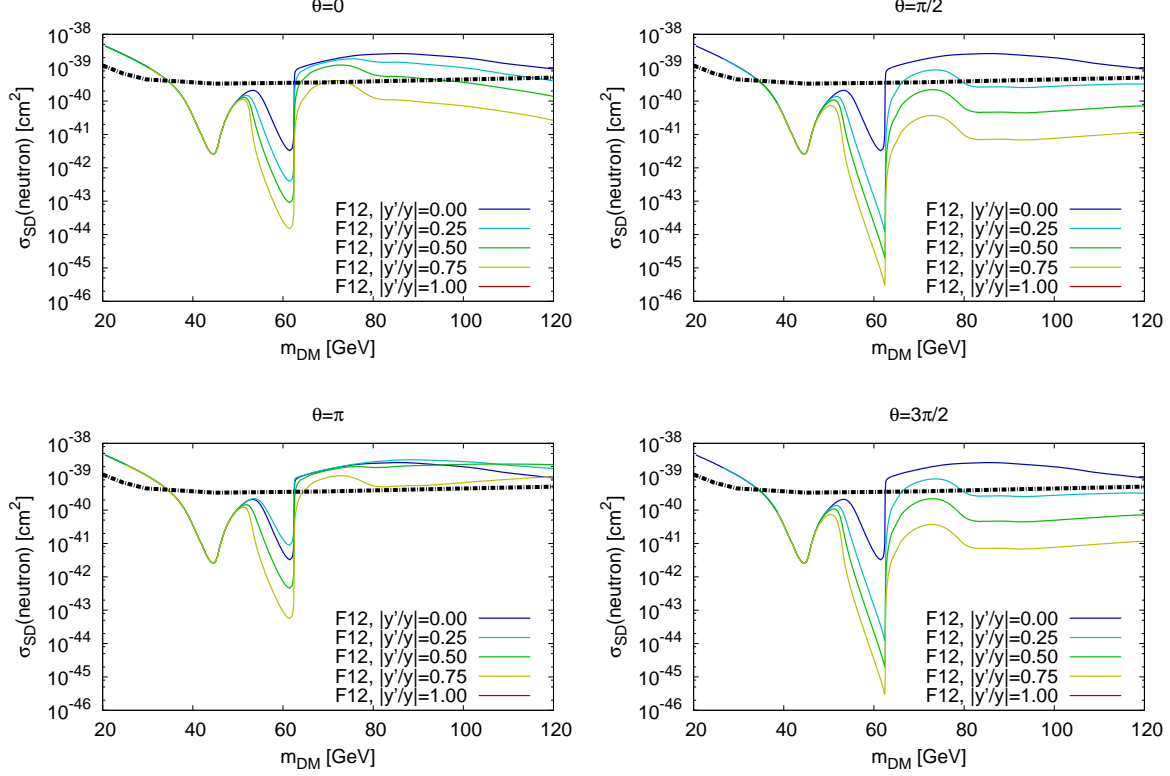


Figure 8: The spin dependent cross section σ_{SD} of model F12. Blue, cyan, green, yellow, and red lines show $|y'/y| = 0, 0.25, 0.5, 0.75$ and 1 respectively. We take $m_D = 200$ GeV in these figures. For model F12, we take $\theta = 0$ (upper left), $\pi/2$ (upper right), π (lower left) and $3\pi/2$ (lower right). We also show σ_{SI} for model S1 (gray line) and model S2 with $m_{S^0} = m_{H^+} = 150$ GeV for references. Black lines shows the constraint on the spin-dependent cross section of neutron-WIMP from XENON 100 [39].

condition is satisfied:

$$\begin{aligned}
 m_{DM} &= m_S = -m_D \sin 2\phi \cos \theta \quad (\theta = 0, \pi), \\
 m_{DM}^2 &= \frac{m_S^2 m_D^2 \sin^2 2\phi \sin^2 \theta}{m_S^2 + m_D^2 \sin^2 2\phi + 2m_S m_D \sin 2\phi \cos \theta} \quad (\theta \neq 0, \pi),
 \end{aligned} \tag{34}$$

where $\tan \phi = |y/y'|$. Here we take $m_S > 0$ and $m_D > 0$ by using the freedom of the field redefinition, thus $\theta = 0$ can not satisfy this condition. When this condition is satisfied, we have a sizable annihilation cross section and small spin independent cross section. Such a parameter region is called as “blind spot” [16].

We also show the spin-dependent direct detection cross section for model F12 given the

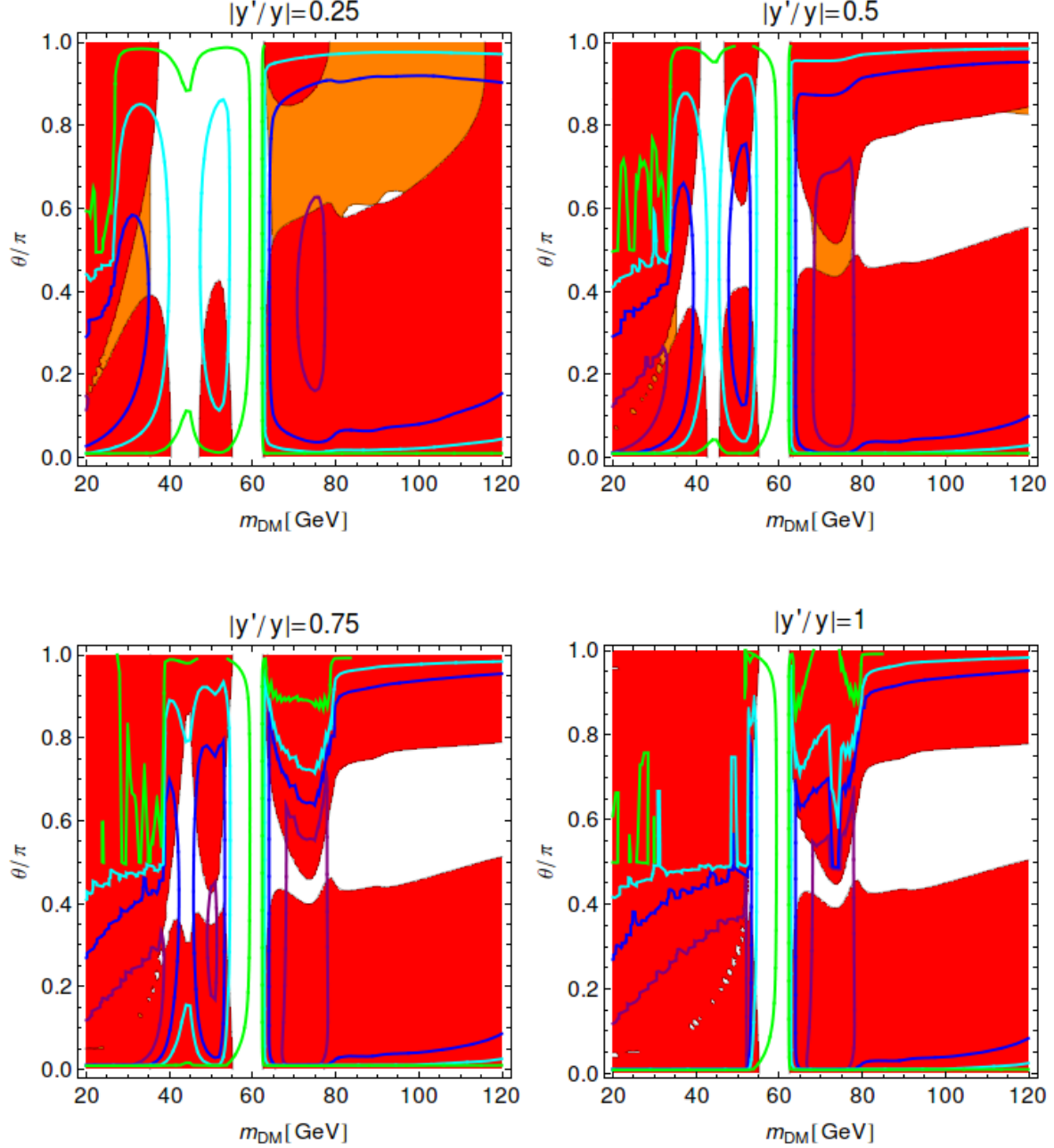


Figure 9: The electron EDM in $m_{\text{DM}}-\theta$ plane. We take $|y'/y| = 0.25, 0.5, 0.75, 1$ in each figure, and $m_D = 200$ GeV in all of the figures. At each point, we set overall size of the Yukawa couplings y and y' to realize $\Omega_{\text{DM}} h^2 = 0.12$. Green, cyan, blue, and purple lines shows $|d_e| = 10^{-30}, 10^{-29}, 3 \times 10^{-29}$ and 9×10^{-29} ecm, respectively. The red regions are excluded by the constraint on the spin-independent cross section by the LUX experiment [26]. The orange regions are not excluded by the LUX but are excluded by the constraint on the spin-dependent cross section by the XENON100 experiment [39].

correct dark matter abundance in Fig. 8. By comparing with Fig. 7, we find that the spin-dependent cross section gives weaker bound than the spin-independent cross section in wide region. Exception is the blind spots. In the blind spots, the dark matter couplings to the Z boson and to the Higgs boson with γ^5 are needed to reproduce the relic abundance, so the coupling to the Z boson can be large enough to make the spin-dependent cross section larger than the current bound. This is crucial in the blind spots for $\theta = \pi$ case because the dark matter couplings to the Higgs boson completely vanish in this case, and thus the dark matter coupling to the Z boson must be sizable. We see this feature in the bottom-left panel in Figs. 7 and 8. In these panels, $\theta = \pi$ and there is a blind spot for $m_{\text{DM}} \simeq 90$ GeV and $|y'/y| = 0.25$, and we find this region is already excluded by the bound on the spin-dependent cross section.

Non-vanishing CP phase significantly enlarges the viable mass range of the dark matter by having y_S and y_P simultaneously. We show in Fig. 9 the contour of the spin-independent cross section for various $|y'/y|$ ratios in the $m_{\text{DM}}-\theta$ plane. As we will see later, such a CP phase induces EDM of the electron, and thus wide range of parameters can be covered by future EDM measurements.

3.3.2 Higgs invisible decay

If the mass of the dark matter is smaller than a half of the Higgs boson mass, the Higgs invisible decay channel opens and we can use it as a probe of the dark matter sector. In Fig. 10, we show the branching fraction of the invisible decay of model F12. We calculate the partial decay width for the invisible decay $\Gamma_{\text{inv.}}$ by using micrOMEGAs. The decay width of the Higgs boson in the SM is calculated as $\Gamma_{\text{SM}} = 4.41 \times 10^{-3}$ GeV for $m_h = 125$ GeV by using HDECAY [40]. The branching fraction of the invisible decay is given by $\Gamma_{\text{inv.}}/(\Gamma_{\text{inv.}} + \Gamma_{\text{SM}})$. In Fig. 10, we vary three parameters, $(\theta, |y'/y|, m_2)$, and their values are

$$\theta/\pi = 0, 0.05, 0.01, \dots, 1.00, \quad (35)$$

$$|y'/y|^{-1} = 1, 1.5, 2.0, \dots, 20.0, \quad (36)$$

$$m_2 = 150, 160, \dots, 500. \quad (37)$$

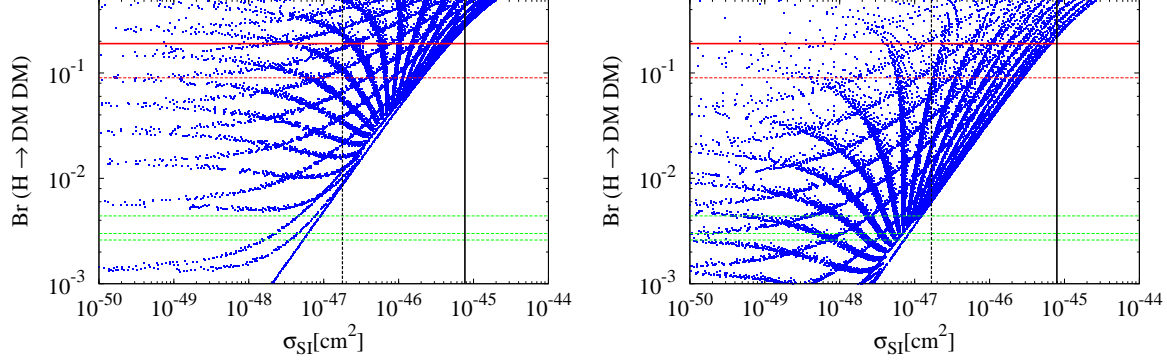


Figure 10: The spin independent cross section versus $\text{Br}(h \rightarrow 2\text{DM})$ for $m_{\text{DM}} = 40$ GeV (left panel) and $m_{\text{DM}} = 45$ GeV (right panel) in model F12. See text for the parameter we used. The red solid line is the current bound [12]. The red dashed line is the future prospect of LHC at 300 fb^{-1} [29]. The three green dashed lines are the future prospect of the ILC. (250 GeV with 250 fb^{-1} , 500 GeV with 500 fb^{-1} , 1 TeV with 1 ab^{-1} [29].) The black solid line is the current bound by the LUX experiment. The black dashed line is the future prospect by XENON1T.

Other parameters are fixed by the dark matter mass and the relic abundance. We find that the smaller spin independent cross section means the smaller branching fraction of the Higgs invisible decay. We also find that the ILC can detect the signal of this model by searching for the Higgs invisible decay even if the XENON1T experiment does not find any dark matter signals. This is different feature of this model from model S1 and S2. Again, by having y_S and y_P coupling simultaneously, the invisible width can be large even if the spin-independent cross section is small.

3.3.3 S and T parameters

The contributions to $\Pi_{VV'}$'s from the dark matter sector are given by,

$$\Pi_{WW} = -\frac{g^2}{16\pi^2} \sum_i \left((|\mathcal{C}_{L,i}|^2 + |\mathcal{C}_{R,i}|^2) H(m_i, m_D) + 4\text{Re}(\mathcal{C}_{L,i}\mathcal{C}_{R,i}^*) m_D m_i B_0(m_i, m_D) \right), \quad (38)$$

$$\begin{aligned} \Pi_{ZZ} = & -\frac{g^2}{c^2} \frac{(1-2s^2)^2}{32\pi^2} \left(H(m_D, m_D) + 2m_D^2 B_0(m_D, m_D) \right) \\ & -\frac{g^2}{c^2} \frac{1}{32\pi^2} \sum_{i,j} \left((|\mathcal{N}_{L,ij}|^2 + |\mathcal{N}_{R,ij}|^2) H(m_i, m_j) + 4\text{Re}(\mathcal{N}_{L,ij}\mathcal{N}_{R,ji}) m_i m_j B_0(m_i, m_j) \right), \end{aligned} \quad (39)$$

$$\Pi_{Z\gamma} = -\frac{eg}{c} \frac{1-2s^2}{16\pi^2} \left(H(m_D, m_D) + 2m_D^2 B_0(m_D, m_D) \right), \quad (40)$$

$$\Pi_{\gamma\gamma} = -\frac{e^2}{8\pi^2} \left(H(m_D, m_D) + 2m_D^2 B_0(m_D, m_D) \right). \quad (41)$$

The definitions of B_0 and H are given in the Appendix A.1. By using the above two-point functions, S and T are calculated by the formulae which are given in Eqs. (24, 25). We show numerical results for S and T parameters in Fig. 11.

3.3.4 Electric dipole moment

In model F12, as we have seen in Sec. 2, the Yukawa couplings of the dark matter can have a CP-violating phase, and thus we can probe dark matter sector by the measurement of EDMs. In this model, two-loop diagram contributes to EDMs and its contribution is given by,³

$$\frac{d_f}{e} = 2T_{3f} \sum_{i=1}^3 \left(\frac{g^2}{16\pi^2} \right)^2 \text{Im}[\mathcal{C}_{L,i}\mathcal{C}_{R,i}^*] \frac{m_i m_D m_f}{m_W^4} \int_0^1 \frac{dx}{x} \frac{\log M_i^2(x)/m_W^2}{M_i^2(x)/m_W^2 - 1}, \quad (42)$$

where $M_i^2(x) = m_i^2/(1-x) + m_D^2/x$. In the limit $m_D \gg m_S$, yv , $y'v$,

$$\frac{d_f}{e} \simeq \frac{\alpha^2 T_{3f} m_f}{64\pi^2 s_W^4} \frac{\text{Im}(yy') v^2 m_S}{m_W^2 m_D^3} \left(\log \frac{m_D^2}{m_W^2} + 1 \right). \quad (43)$$

Numerically,

$$d_e \simeq 8.6 \times 10^{-30} e \text{ cm} \times \text{Im}(yy') \left(\frac{m_S}{100 \text{ GeV}} \right) \left(\frac{m_D}{1000 \text{ GeV}} \right)^{-3} \left(\log \frac{m_D^2}{m_W^2} + 1 \right). \quad (44)$$

³We have checked that our calculation is consistent with Ref. [43].

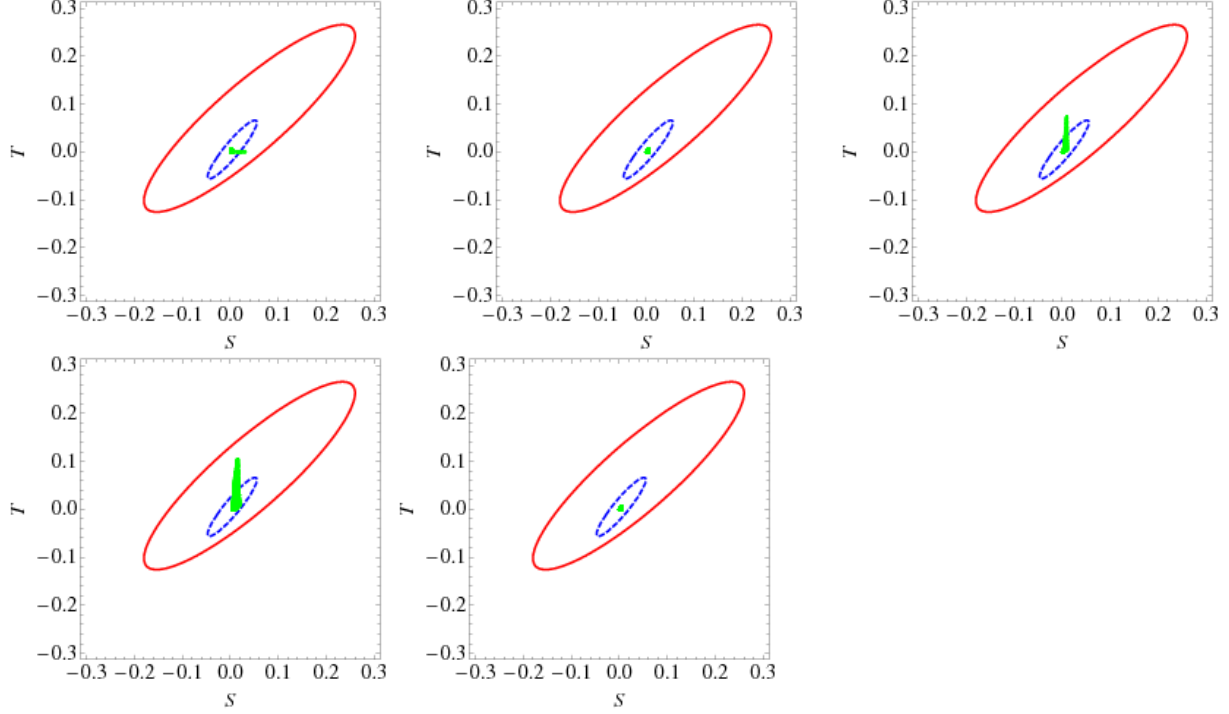


Figure 11: The S and T parameters for $m_{\text{DM}} = 40$ GeV (upper-left), $m_{\text{DM}} = 45$ GeV (upper-middle), $m_{\text{DM}} = 60$ GeV (upper-right), $m_{\text{DM}} = 70$ GeV (lower-left), $m_{\text{DM}} = 200$ GeV (lower-right). Red line is current bound at 95% C.L. [41]. Blue dashed line is GFITTER’s future prospect at the ILC [42]. The green dots are consistent points with the current direct search result by the LUX experiment.

Constraint on the electron EDM is given by the ACME experiment [44],

$$|d_e| < 8.7 \times 10^{-29} e \text{ cm} \quad (90\% \text{ C.L.}) \quad (45)$$

In Fig. 9, we show the non-zero CP violating phase opens large parameter space to avoid the constraints from the direct detection experiments. The figure shows the electron EDM measurement is very useful to probe such a region. We show the numerical result of electron EDM in Fig. 12 with future prospects [45, 46, 47].

In the upper panel in Fig. 12, we also show the branching fraction of the Higgs invisible decay. The red region is already excluded at the LHC [12]. The blue region is within the reach of the LHC [29]. The cyan region will be searched by the ILC experiment [29]. We find that the ILC has the capability to seek the parameter region where both dark matter direct detection experiments and EDM experiments cannot access.

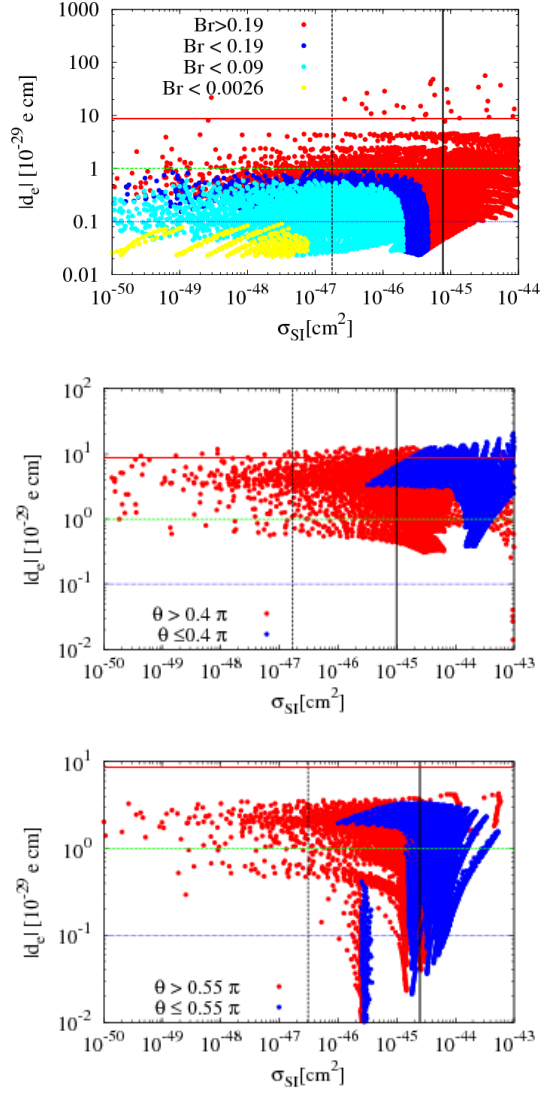


Figure 12: The spin independent cross section versus the electron EDM for $m_{DM} = 40$ GeV (upper), 70 GeV (middle) and $m_{DM} = 200$ GeV (lower). The red solid line is the current bound from ACME experiment. The green and blue dashed lines are future prospects [45, 47]. The black solid line is the current bound by the LUX experiment. The black dashed line is the future prospect by XENON1T.

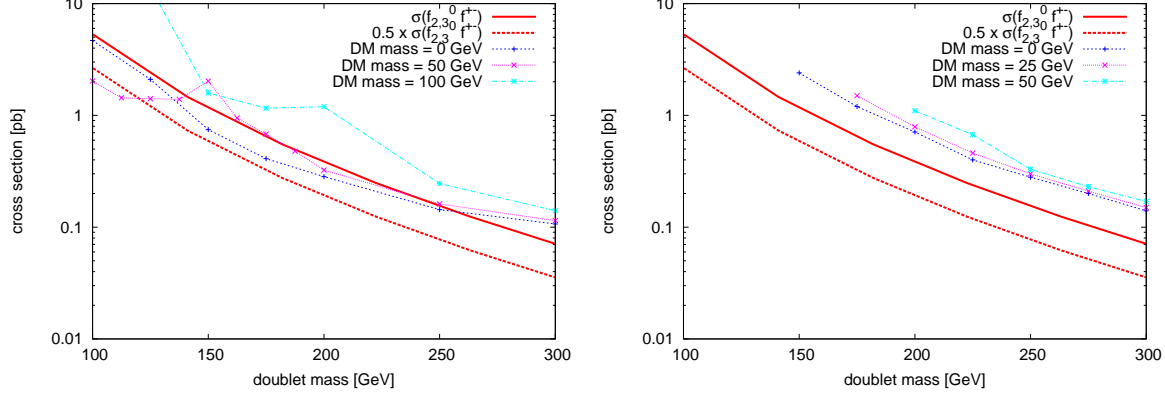


Figure 13: Constraint on production cross section of $f_{2,3}^0 f^\pm$ at the LHC $\sqrt{s} = 8$ TeV. Left figure shows the tripleton search [48], right figure shows the one lepton with two b -jets search [49].

3.3.5 Direct search

In the case $m_S, yv, y'v \ll m_D$, f_2^0 , f_3^0 and f^\pm approximately forms $SU(2)$ doublet, and their masses are almost degenerated. The main decay modes of heavy matters are $f_{2,3}^0 \rightarrow f_1(h/Z)$ and $f^\pm \rightarrow f_1 W^\pm$. The main production channel at the LHC is $pp \rightarrow f_{2,3}^0 f^\pm \rightarrow f_1 f_1 W^\pm (Z/h)$. Such channels are searched in a context of electroweakino search in supersymmetric models. The most sensitive channels are the tripleton mode [48] and the one-lepton with two b -jets mode [49]. The former mode makes the constraint on $\sum_i \sigma(pp \rightarrow f_i^0 f^\pm) \text{Br}(f_i^0 \rightarrow f_1 Z) \text{Br}(f^\pm \rightarrow f_1 W^\pm)$, and the latter $\sum_i \sigma(pp \rightarrow f_i^0 f^\pm) \text{Br}(f_i^0 \rightarrow f_1 h) \text{Br}(f^\pm \rightarrow f_1 W^\pm)$. We estimated the production cross section by using Prospino2 [50] by taking pure Higgsino limit. In Fig. 13, we show the present status of constraint from direct search on model F12. Ref. [51] shows that $m_{\text{wino}} \lesssim 800$ GeV can be probed by tripleton search at LHC 14 TeV 3000 fb^{-1} for wino, *i.e.*, $SU(2)$ triplet Majorana fermion. Since the production cross section of $f_{2,3}^0 f^\pm$ in model F12 is a half of the cross section for the pair production of a neutral wino and a charged wino, we expect $m_D \lesssim 600\text{--}700$ GeV can be probed LHC 14 TeV 3000 fb^{-1} .

3.4 Model F23

Here, we discuss the phenomenology of model F23. As we will see later, the measurement of the Higgs diphoton signal gives a severe constraint on the model.

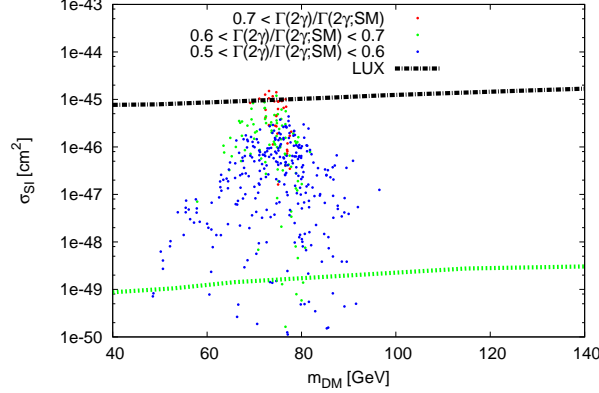


Figure 14: Scatter plot of $m_{\text{DM}}\text{-}\sigma_{\text{SI}}$ for model F23. Black and green lines are same as Fig. 3. Red points satisfies $\mu(h \rightarrow 2\gamma) > 0.7$, and at green and blue points, $0.6 < \mu(h \rightarrow 2\gamma) < 0.7$, $0.5 < \mu(h \rightarrow 2\gamma) < 0.6$, respectively.

3.4.1 Relic abundance and direct detection

We show the dark matter mass and the spin independent cross section in Fig. 14. In this plot, we take parameters of the model as $\lambda, \lambda' \in [0, 1.5]$, $m_D, m_T \in [0, 400]$ GeV and $\theta \in [0, \pi]$. We calculate $\Omega_{\text{DM}}h^2$, and extract the points which satisfy $0.1 \leq \Omega_{\text{DM}}h^2 \leq 0.15$.

3.4.2 Higgs diphoton decay signal

Here, we show the Higgs diphoton signal strength. The interaction terms of charged fermion χ 's are given by,

$$\mathcal{L} = -y_{S,i}h\bar{\Psi}_i^+\Psi_i - iy_{P,i}h\bar{\Psi}_i^+\gamma^5\Psi_i^+, \quad (46)$$

where the couplings $y_{S,i}$ and $y_{P,i}$ are determined by λ, λ', U^+ and U^- in Eq. (21). The decay width of $h \rightarrow \gamma\gamma$ is given by,

$$\Gamma(h \rightarrow \gamma\gamma) = \frac{G_F\alpha^2 m_h^3}{128\sqrt{2}\pi^3} \left(\left| A_{\text{SM}} + \sum_i \frac{y_{S,i}v}{m_{\chi_i^\pm}} A_{1/2}^H \left(\frac{m_h^2}{4m_{\chi_i^\pm}^2} \right) \right|^2 + \left| \sum_i \frac{y_{P,i}v}{m_{\chi_i^\pm}} A_{1/2}^A \left(\frac{m_h^2}{4m_{\chi_i^\pm}^2} \right) \right|^2 \right). \quad (47)$$

We show how the diphoton branching fraction is modified in Fig. 15. In this plot, we take the parameters of the model as $\lambda, \lambda' \in [0, 1.5]$, $m_D, m_T \in [0, 400]$ GeV and $\theta \in [0, \pi]$. Then we calculate $\Omega_{\text{DM}}h^2$ and extract the points which satisfy $0.1 \leq \Omega_{\text{DM}}h^2 \leq 0.15$. We

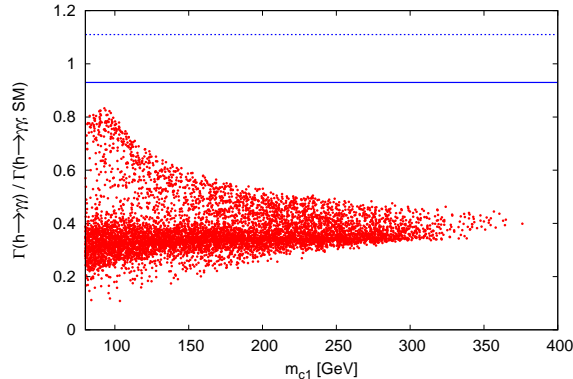


Figure 15: Diphoton signal strength and mass of the lightest charged fermion in model F23. The region above dotted (solid) blue line is consistent with the measurement of $h \rightarrow \gamma\gamma$ within 1σ (2σ) deviation.

use the constraint on $m_{\chi_1^\pm}$ by the chargino search at the LEP experiment [52, 53, 54, 55], $m_{\chi_1^\pm} \lesssim 93$ GeV. Applying this constraint, we can see from Fig. 15 that the diphoton signal strength is deviated from the SM value, $\mu(h \rightarrow 2\gamma) < 0.85$. However, the diphoton signal strength measured at the LHC is $\mu(h \rightarrow 2\gamma) = 1.29 \pm 0.18$ (95 % C.L.)⁴. Therefore, this model is already excluded by LEP2 and LHC. Hence, we do not investigate this model further in this paper.

4 Discrimination of model S1 and F12

So far, we have discussed four dark matter models which are listed in Tab. 1. Model S2 predicts ~ 10 % deviation of $\mu(h \rightarrow 2\gamma)$ from the SM, and the light mass region, $m_{\text{DM}} < 72$ GeV, will be covered at the ILC. On the other hand, model S1 and model F12 do not predict a deviation in Higgs diphoton signal strength, and we can distinguish them from model S2. Model F23 predicts too large deviation of $\mu(h \rightarrow 2\gamma)$ from the SM, and it is already excluded.

The difference between model S1 and F12 is very subtle because the phenomenology of dark matter in model S1 and F12 is quite similar. If direct search experiments will discover the dark matter, and if the dark matter mass and its spin independent cross

⁴This value is obtained from naive combination of $1.65^{+0.33}_{-0.28}$ from the ATLAS collaboration [56] and $1.14 \pm 0.21(\text{stat.})^{+0.09}_{-0.05}(\text{syst.})^{+0.13}_{-0.09}(\text{theo.})$ from the CMS collaboration [57].

section are consistent with the prediction of model S1, then we will have to discriminate model S1 from F12 by using some other combination of observables. In this section, we discuss discrimination of model S1 and F12 for each mass region.

4.1 $m_{\text{DM}} \lesssim 53 \text{ GeV}$

In this mass region, as we can see from Fig. 7, model S1 is already excluded by the dark matter direct search while model F12 is not. Therefore we can distinguish these two models in this mass region by the dark matter direct search.

4.2 $53 \text{ GeV} \lesssim m_{\text{DM}} \lesssim m_h/2$

We show the correlations among the spin independent cross section, the electron EDM, and the branching fraction of the Higgs invisible decay in Fig. 16. Here we take $m_{\text{DM}} = 55 \text{ GeV}$ as a benchmark. In these plots, for given m_{DM} and m_D , we take $|y/y'| \in [0, 1]$ and $\theta \in [0, \pi]$ and take overall size of y and y' to choose one which gives $\Omega_{\text{DM}} h^2 = 0.1196$. In model F12 with m_D to be $\mathcal{O}(100) \text{ GeV}$, this model gives various observables. Obviously, the electron EDM is a powerful tool for discrimination between S1 and F12 because model S1 does not include new CP violation source and does not predict any EDMs. We also show the case if future experiments [46, 47] do not observed electron EDM in Fig. 17. In this case, the branching fraction of the Higgs invisible decay is helpful to distinguish two models. The model F12 predicts wide range of the invisible width, while model S1 is a point.

We also check the case with $m_{\text{DM}} = 60 \text{ GeV}$. In this case, both the electron EDM and the branching fraction of the Higgs invisible decay are smaller than the future prospect, and we have to rely on the direct search of the exotic particles other than the dark matter particle in model F12 in order to discriminate model S1 and F12.

4.3 $100 \text{ GeV} \lesssim m_{\text{DM}}$

In the case of $m_{\text{DM}} = 100 \text{ GeV}$, we show a scatter plot on the $\sigma_{\text{SI}}-d_e$ plane and $\sigma_{\text{SI}}-S$ plane in Fig. 18. In these plots, for given m_{DM} and m_D , we take $|\lambda/\lambda'| \in [0, 1]$ and $\theta \in [0, \pi]$ and take overall size of λ and λ' to choose one which gives $\Omega_{\text{DM}} h^2 = 0.1196$. Here, we can

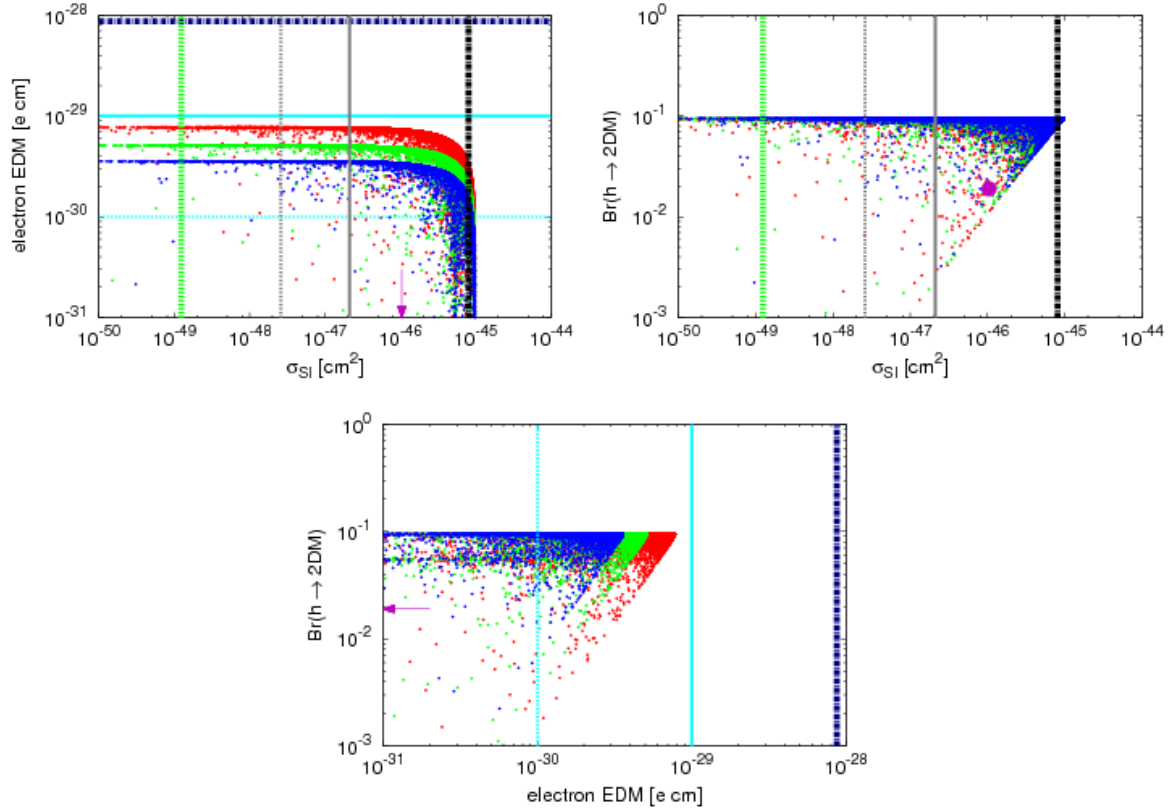


Figure 16: Discrimination of dark matter models for $m_{\text{DM}} = 55$ GeV. Red, green, and blue points show $m_D = 200$, 300 and 400 GeV, respectively. Magenta points or arrows show model S1. Black chain line is constraint from the LUX, and gray solid and dotted line shows the future prospects of XENON1T and LZ experiment, respectively. The values of experimental reach are taken from Ref. [27]. Green dotted line shows the discovery limit which is caused by atmospheric and astrophysical neutrinos. Blue chain line shows the constraint from ACME experiment. Solid turquoise line shows future prospect of measurement of Fr atom [45]. Dotted turquoise line shows future prospect of measurement of YbF molecule and WN ion [46, 47].

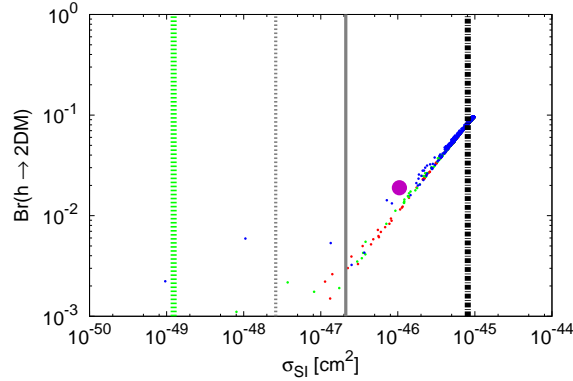


Figure 17: Discrimination of dark matter models for $m_{\text{DM}} = 55$ GeV in a parameter region with $|d_e| < 10^{-30} \text{ecm}$, *i.e.*, in this case, future experiment [46, 47] cannot observe electron EDM. The meaning of the lines and dot are the same as Fig. 16.

see that the electron EDM is very useful tools for the discrimination of the models.

5 Conclusion and discussions

In this paper, we considered several simple dark matter models, and studied their phenomenological aspects comprehensively. In particular, we discussed prospects of experimental reach to the dark matter models and discrimination of them for the case of dark matter mass is smaller than $\mathcal{O}(100)$ GeV.

In this mass region, model S2 predicts 10% deviation of $\mu(h \rightarrow 2\gamma)$, and thus the most of the region for the light dark matter in model S2 can be covered by the LHC and the ILC. Model F23 predicts large $\mu(h \rightarrow 2\gamma)$ deviation and already excluded. For model F12, in the case of the doublet Dirac mass m_D to be a few hundred GeV, the observation of the electron EDM and the discovery of the direct search for doublet fermions are expected. For $53 \text{ GeV} < m_{\text{DM}} < m_h/2$ and $100 \text{ GeV} < m_{\text{DM}}$, if the electron EDM is not observed, it is not easy task to distinguish model S1 and F12, because the spin-independent cross section for model F12 can mimic the one for model S1 due to the existence of the blind spots. The measurements of the branching fraction of the Higgs invisible decay at the ILC provide us with useful information in the case. Of course, the direct search for other Z_2 odd particles is also useful to distinguish model S1 and F12. We summarize the features of each models for light dark matter in Tab. 2, and current status of the dark matter mass

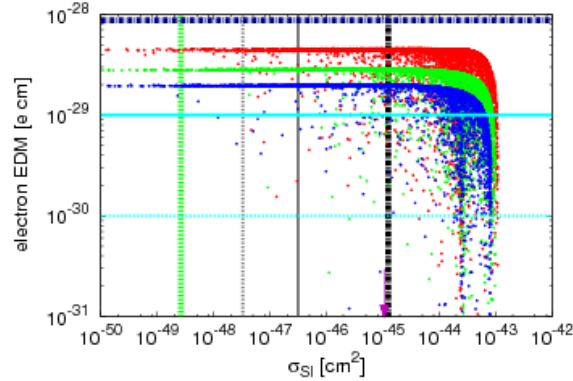


Figure 18: Scatter plot of $\sigma_{\text{SI}}-d_e$ plane and $\sigma_{\text{SI}}-S$ plane for $m_{\text{DM}} = 100$ GeV. Red, green and blue points shows $m_D = 200, 300$ and 400 GeV, respectively. Magenta points or arrows show model S1. For the explanation of black, green, blue, turquoise lines, see the caption of Fig. 16.

Table 2: Summary of light dark matter. The cells marked “-” are not treated in this paper.

	S1	S2	F12	F23
$\mu(h \rightarrow 2\gamma)$	1 (same as SM)	~ 0.9	1 (same as SM)	$\lesssim 0.8$
EWPT	(same as SM)			-
EDM	(same as SM)	(same as SM)	$> 10^{-30} e \text{ cm}$ is possible	-
Collider	-	-	LHC	-

region in Fig. 19. We also summarize how to distinguish light dark matter models which we addressed in this paper in Fig. 20.

Acknowledgements

This work is supported by JSPS Grant-in-Aid for Young Scientists (B) (No. 23740165 [RK]), MEXT Grant-in-Aid for Scientific Research on Innovative Areas (No. 25105011 [RK] and No. 23104006 [TA]) and JSPS Research Fellowships for Young Scientists [RS].

A Loop functions

Here, we summarize the loop functions which are used in the calculation of EWPT and diphoton signal strength.

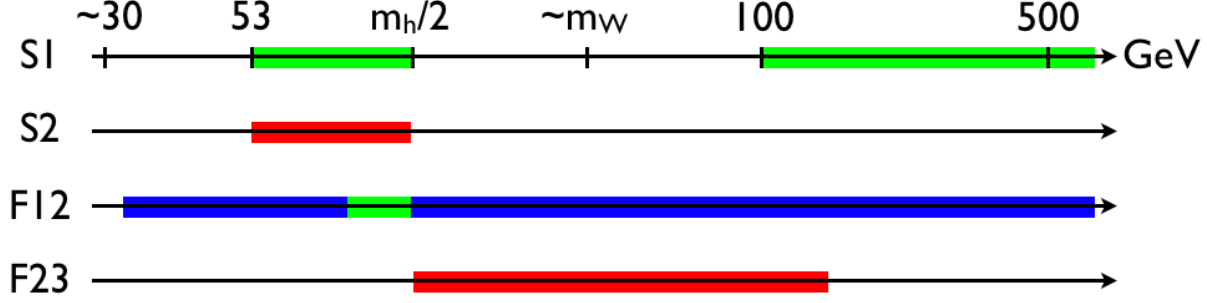


Figure 19: Summary of the current status of each models in the light dark matter mass region. The color shaded regions are consistent with LUX experiments. The red shaded regions predict smaller diphoton signal strength. The blue shaded regions predict EDM.

A.1 Loop functions for oblique corrections

Scalar loop contribution to vector boson two-point function is given as,

$$\begin{aligned} & \mu^{4-d} \left[\int \frac{d^d k}{(2\pi)^d} \frac{(2k+p)^\mu (2k+p)^\nu}{[(k+p)^2 - m_1^2][k^2 - m_2^2]} + \int \frac{d^d k}{(2\pi)^d} \frac{g^{\mu\nu}}{k^2 - m_1^2} + \int \frac{d^d k}{(2\pi)^d} \frac{g^{\mu\nu}}{k^2 - m_2^2} \right] \\ &= \frac{i}{16\pi^2} 4\tilde{B}_{22}(m_1, m_2) g^{\mu\nu} + (p^\mu p^\nu \text{ terms}). \end{aligned} \quad (48)$$

Fermion loop contribution to vector boson two-point function is given as,

$$\begin{aligned} & (-1)\mu^{4-d} \int \frac{d^d k}{(2\pi)^d} \int \text{tr} \left[\gamma^\mu (g_L P_L + g_R P_R) \frac{\not{k} + \not{p} + m_1}{(k+p)^2 - m_1^2} \gamma^\nu (h_L P_L + h_R P_R) \frac{\not{k} + m_2}{k^2 - m_2^2} \right] \\ &= \frac{-i}{16\pi^2} \left[(g_L h_L + g_R h_R) H(m_1, m_2) + 2(g_L h_R + g_R h_L) m_1 m_2 B_0(m_1, m_2) \right] g^{\mu\nu} + \dots \end{aligned} \quad (49)$$

Here, \dots represents terms which are proportional to $p^\mu p^\nu$. If internal fermion is same Majorana fermion, Eq. (49) accompanies with symmetric factor $1/2$. B_0 , H and \tilde{B}_{22} are loop functions given in Ref. [58], and their integral forms are,

$$B_0(m_1, m_2) = \frac{1}{\hat{\epsilon}} - \int_0^1 dx \log \frac{\Delta}{\mu^2}, \quad (50)$$

$$H(m_1, m_2) = \frac{1}{\hat{\epsilon}} \left(\frac{2}{3} p^2 - m_1^2 - m_2^2 \right) - \int_0^1 dx \left(4x(1-x)p^2 - 2xm_1^2 - 2(1-x)m_2^2 \right) \log \frac{\Delta}{\mu^2}, \quad (51)$$

$$\tilde{B}_{22}(m_1, m_2) = -\frac{1}{\hat{\epsilon}} \frac{p^2}{12} + \frac{1}{4} \int_0^1 dx \left((1-2x)^2 p^2 - (m_1^2 - m_2^2)(1-2x) \right) \log \frac{\Delta}{\mu^2}. \quad (52)$$

where $\Delta = xm_1^2 + (1-x)m_2^2 - x(1-x)p^2 - i\epsilon$, $\hat{\epsilon} = 2 - d/2$ and μ is the renormalization scale in $\overline{\text{MS}}$ scheme.

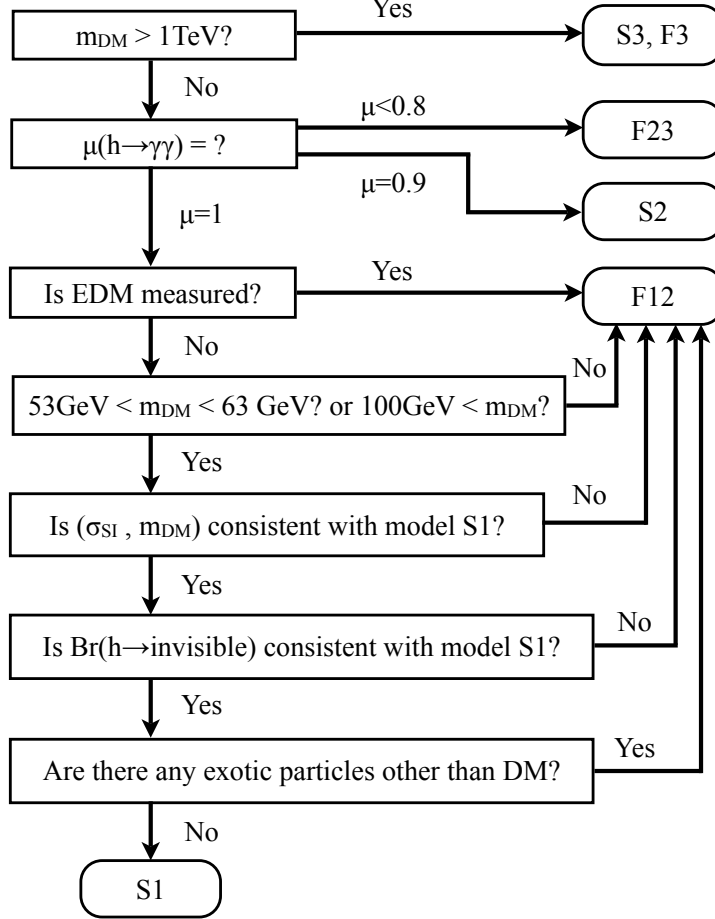


Figure 20: Model chromatography for light dark matter models. We consider model S1, S2, S3, F12, F23, and F3. Here, we assume that only DM sector particles give contributions to electron EDM and deviation of diphoton signal strength from SM value.

A.2 Loop functions for diphoton signal

A 's are loop functions which are defined in Ref. [37]. They are defined as,

$$A_1(\tau) = -\tau^{-2}(2\tau^2 + 3\tau + 3(2\tau - 1)f(\tau)), \quad (53)$$

$$A_{1/2}^A(\tau) = 2\tau^{-1}f(\tau), \quad (54)$$

$$A_{1/2}^H(\tau) = 2\tau^{-2}(\tau + (\tau - 1)f(\tau)), \quad (55)$$

$$A_0(\tau) = -\tau^{-2}(\tau - f(\tau)), \quad (56)$$

where $f(\tau)$ is defined as,

$$f(\tau) = \begin{cases} \arcsin^2 \sqrt{\tau}. & (\tau \leq 1) \\ -\frac{1}{4} \left(\log \frac{1 + \sqrt{1 - \tau^{-1}}}{1 - \sqrt{1 - \tau^{-1}}} - i\pi \right)^2. & (\tau > 1) \end{cases} \quad (57)$$

References

- [1] J. Oort, Bull. Astr. Inst. Netherlands. **6**, 249 (1932).
- [2] F. Zwicky, Helv. Phys. Acta **6**, 110 (1933).
- [3] G. Steigman and M. S. Turner, Nucl. Phys. B **253**, 375 (1985).
- [4] V. Silveira and A. Zee, Phys. Lett. B **161**, 136 (1985).
- [5] J. McDonald, Phys. Rev. D **50**, 3637 (1994) [hep-ph/0702143 [HEP-PH]].
- [6] C. P. Burgess, M. Pospelov and T. ter Veldhuis, Nucl. Phys. B **619**, 709 (2001) [hep-ph/0011335].
- [7] J. M. Cline, K. Kainulainen, P. Scott and C. Weniger, Phys. Rev. D **88**, 055025 (2013) [arXiv:1306.4710 [hep-ph]].
- [8] N. G. Deshpande and E. Ma, Phys. Rev. D **18**, 2574 (1978).
- [9] R. Barbieri, L. J. Hall and V. S. Rychkov, Phys. Rev. D **74**, 015007 (2006) [hep-ph/0603188].
- [10] A. Arhrib, Y. L. S. Tsai, Q. Yuan and T. C. Yuan, JCAP **1406**, 030 (2014) [arXiv:1310.0358 [hep-ph]].
- [11] M. Krawczyk, D. Sokolowska and B. Swiezewska, arXiv:1304.7757 [hep-ph].
- [12] G. Belanger, B. Dumont, U. Ellwanger, J. F. Gunion and S. Kraml, Phys. Rev. D **88**, 075008 (2013) [arXiv:1306.2941 [hep-ph]].
- [13] T. Araki, C. Q. Geng and K. I. Nagao, Phys. Rev. D **83**, 075014 (2011) [arXiv:1102.4906 [hep-ph]].
- [14] M. Cirelli, A. Strumia and M. Tamburini, Nucl. Phys. B **787**, 152 (2007) [arXiv:0706.4071 [hep-ph]].

- [15] T. Cohen, J. Kearney, A. Pierce and D. Tucker-Smith, Phys. Rev. D **85**, 075003 (2012) [arXiv:1109.2604 [hep-ph]].
- [16] C. Cheung and D. Sanford, JCAP **1402**, 011 (2014) [arXiv:1311.5896 [hep-ph]].
- [17] A. Dedes and D. Karamitros, Phys. Rev. D **89**, 115002 (2014) [arXiv:1403.7744 [hep-ph]].
- [18] P. A. R. Ade *et al.* [Planck Collaboration], Astron. Astrophys. (2014) [arXiv:1303.5076 [astro-ph.CO]].
- [19] M. Cirelli, N. Fornengo and A. Strumia, Nucl. Phys. B **753**, 178 (2006) [hep-ph/0512090].
- [20] L. Randall and R. Sundrum, Nucl. Phys. B **557**, 79 (1999) [hep-th/9810155].
- [21] G. F. Giudice, M. A. Luty, H. Murayama and R. Rattazzi, JHEP **9812**, 027 (1998) [hep-ph/9810442].
- [22] A. Alloul, N. D. Christensen, C. Degrande, C. Duhr and B. Fuks, Comput. Phys. Commun. **185**, 2250 (2014) [arXiv:1310.1921 [hep-ph]].
- [23] G. Belanger, F. Boudjema, A. Pukhov and A. Semenov, Comput. Phys. Commun. **185**, 960 (2014) [arXiv:1305.0237 [hep-ph]].
- [24] G. Aad *et al.* [ATLAS Collaboration], Phys. Rev. D **90**, 052004 (2014) [arXiv:1406.3827 [hep-ex]].
- [25] CMS Collaboration [CMS Collaboration], and studies of the compatibility of its couplings with the standard model,” CMS-PAS-HIG-14-009.
- [26] D. S. Akerib *et al.* [LUX Collaboration], Phys. Rev. Lett. **112**, 091303 (2014) [arXiv:1310.8214 [astro-ph.CO]].
- [27] J. L. Feng, S. Ritz, J. J. Beatty, J. Buckley, D. F. Cowen, P. Cushman, S. Dodelson and C. Galbiati *et al.*, arXiv:1401.6085 [hep-ex].
- [28] J. Billard, L. Strigari and E. Figueroa-Feliciano, Phys. Rev. D **89**, 023524 (2014) [arXiv:1307.5458 [hep-ph]].
- [29] H. Baer, T. Barklow, K. Fujii, Y. Gao, A. Hoang, S. Kanemura, J. List and H. E. Logan *et al.*, arXiv:1306.6352 [hep-ph].

- [30] M. Klasen, C. E. Yaguna and J. D. Ruiz-Alvarez, Phys. Rev. D **87**, 075025 (2013) [arXiv:1302.1657 [hep-ph]].
- [31] A. Pierce and J. Thaler, JHEP **0708**, 026 (2007) [hep-ph/0703056 [HEP-PH]].
- [32] E. Lundstrom, M. Gustafsson and J. Edsjo, Phys. Rev. D **79**, 035013 (2009) [arXiv:0810.3924 [hep-ph]].
- [33] E. Dolle, X. Miao, S. Su and B. Thomas, Phys. Rev. D **81**, 035003 (2010) [arXiv:0909.3094 [hep-ph]].
- [34] X. Miao, S. Su and B. Thomas, Phys. Rev. D **82**, 035009 (2010) [arXiv:1005.0090 [hep-ph]].
- [35] M. E. Peskin and T. Takeuchi, Phys. Rev. D **46**, 381 (1992).
- [36] A. Arhrib, R. Benbrik and N. Gaur, Phys. Rev. D **85**, 095021 (2012) [arXiv:1201.2644 [hep-ph]].
- [37] A. Djouadi, Phys. Rept. **457**, 1 (2008) [hep-ph/0503172].
- [38] M. E. Peskin, arXiv:1207.2516 [hep-ph].
- [39] P. Beltrame [XENON Collaboration], arXiv:1305.2719 [astro-ph.CO].
- [40] A. Djouadi, J. Kalinowski and M. Spira, Comput. Phys. Commun. **108**, 56 (1998) [hep-ph/9704448].
- [41] J. Beringer *et al.* [Particle Data Group Collaboration], Phys. Rev. D **86**, 010001 (2012).
- [42] M. Baak *et al.* [Gfitter Group Collaboration], Eur. Phys. J. C **74**, 3046 (2014) [arXiv:1407.3792 [hep-ph]].
- [43] G. F. Giudice and A. Romanino, Phys. Lett. B **634**, 307 (2006) [hep-ph/0510197].
- [44] J. Baron *et al.* [ACME Collaboration], Science **343**, no. 6168, 269 (2014) [arXiv:1310.7534 [physics.atom-ph]].
- [45] Y. Sakemi, K. Harada, T. Hayamizu, M. Itoh, H. Kawamura, S. Liu, H. S. Nataraj and A. Oikawa *et al.*, J. Phys. Conf. Ser. **302**, 012051 (2011).
- [46] D. M. Kara, I. J. Smallman, J. J. Hudson, B. E. Sauer, M. R. Tarbutt and E. A. Hinds, New J. Phys. **14**, 103051 (2012) [arXiv:1208.4507 [physics.atom-ph]].

- [47] D. Kawall, J. Phys. Conf. Ser. **295**, 012031 (2011).
- [48] The ATLAS Collaboration, ATLAS-CONF-2013-035.
- [49] The ATLAS Collaboration, ATLAS-CONF-2013-093.
- [50] W. Beenakker, R. Hopker and M. Spira, hep-ph/9611232.
- [51] The ATLAS Collaboration, ATL-PHYS-PUB-2014-010.
- [52] A. Heister *et al.* [ALEPH Collaboration], Phys. Lett. B **533**, 223 (2002) [hep-ex/0203020].
- [53] G. Abbiendi *et al.* [OPAL Collaboration], Eur. Phys. J. C **29**, 479 (2003) [hep-ex/0210043].
- [54] J. Abdallah *et al.* [DELPHI Collaboration], Eur. Phys. J. C **34**, 145 (2004) [hep-ex/0403047].
- [55] LEP2 SUSY Working Group,
http://lepsusy.web.cern.ch/lepsusy/www/inoslowdmsummer02/charginolowdm_pub.html
- [56] The ATLAS Collaboration, ATLAS-CONF-2014-009.
- [57] V. Khachatryan *et al.* [CMS Collaboration], arXiv:1407.0558 [hep-ex].
- [58] D. M. Pierce, J. A. Bagger, K. T. Matchev and R. j. Zhang, Nucl. Phys. B **491**, 3 (1997) [hep-ph/9606211].